

Gain/Loss-free Non-Hermitian Metamaterials

Maopeng Wu,^{1,*} Mingze Weng,^{1,*} Zhonghai Chi,² Siyong Zheng,² Fubei Liu,² Weijia Luo,² Qian Zhao,^{1,†} Yonggang Meng,¹ and Ji Zhou^{2,‡}

¹*State Key Laboratory of Tribology in Advanced Equipment,
Department of Mechanical Engineering, Tsinghua University, Beijing 100084, China*

²*State Key Laboratory of New Ceramics and Fine Processing,
School of Materials Science and Engineering, Tsinghua University, Beijing 100084, China*

(Dated: April 22, 2025)

The ease of using optical gain/loss provides a fertile ground for experimental explorations of non-Hermitian (NH) physics. Without gain/loss, can we realize the NH effect in a Hermitian system? The interface between the coupled Hermitian subsystems is a natural object for NH physics due to the nonconservative process on it. However, it is still far from enduing the interface with rich NH physics. Here, a junction between the topological insulator and the conductor is considered, where the interface can be effectively described by a NH Hamiltonian—such NH character is ascribed to the conductor self-energy of a reservoir. As a consequence of that, we show the wave propagation along the interface exhibits dissipative non-reciprocity (dubbed non-Bloch transport), which was believed to be unique in NH systems. Moreover, the meta-materialization of tight-binding models is also studied by identifying their equivalent connectivity, enabling us to demonstrate the above exotic NH behavior of the interface experimentally. Our work provides a conceptually rich avenue to construct NH systems for both optics and electronics.

I. INTRODUCTION

Beyond merely being a perturbation, non-Hermitian (NH) contribution to a system can drastically alter its behavior compared to its Hermitian counterpart. One example of this striking phenomenon is the emergence of exceptional points [1], at which both eigenvalues and their associated eigenvectors coalesce [2, 3]. In parallel with those developments, the advent of extending topological phases to NH systems reveals a plethora of unique aspects [4–6], such as anomalous bulk-boundary correspondences accompanied by the NH skin effect [7–11]. It was widely believed that those phenomena are unique to NH systems.

On the other hand, optics and photonics have proven to be the ideal experimental platform to observe the rich physics of NH systems [12–17]. This is because that gain (e.g., gain implemented through simulated emission [18]) and loss (e.g., material absorption [19]) in photonics provide the essential ingredients to construct NH systems in a controllable manner. Under this spirit, recent researches resort to investigating other optical nonconservative processes which can be effectively described by gain/loss, such as the radiation leakage to the surroundings [20], virtual gain [21–23], NH parametric processes [24].

Can we realize the NH effect in a Hermitian system involving neither gain nor loss? An affirmative answer is obtained in this work, demonstrating the gain/loss or the non-Hermiticity of a system is *not* the necessary condition for NH effects. By definition, the NH terms in the

Hamiltonian root in the nonconservative process. So, in principle, the interface between two interacting subsystems is an ideal object for NH physics given the frequent energy and matter flux passing through it. Consequently, it is expected that the NH effect occurs even if the total system comprising subsystems is Hermitian.

However, the interface should be carefully constructed so that its effective Hamiltonian fulfills the mathematical requirement for NH exotic effects, for example, asymmetric hopping in the NH non-Bloch transport [7–9]. Correspondingly, the interface between a topological insulator and a conductor is studied here. This interface has one dimension lower than its constituents, and its effective Hamiltonian consists of: (i) the gapless edge state Hermitian Hamiltonian of the topological insulator; and (ii) the NH self-energy of the conductor that is considered to be a thermal reservoir. As a result, the hopping terms in the effective Hamiltonian are asymmetric due to the unidirectional property of the edge states.

Here, more explicitly, we study a junction of the Haldane model coupled with a conductor. We theoretically show that this interface Hamiltonian is Hatano-Nelson-like and hopping between lattice sites is asymmetric, leading to the non-Bloch transmission. The experimental realization of this junction poses another challenge since the model is based on the tight-binding approximation. Accordingly, we discuss the electromagnetic meta-materialization of this by analyzing the equivalent site (or node) connectivity between the tight-binding model and the proposed metamaterial, and the results from experiment designed under this scheme are consistent with our prediction of the non-Bloch behavior on the interface. The proposed junction model together with the meta-materialization extends the scope of NH photonics or NH metamaterials.

* These two authors contributed equally.

† zhaoqian@tsinghua.edu.cn

‡ zhouji@tsinghua.edu.cn

II. NON-BLOCH TRANSPORT IN THE HERMITIAN SYSTEM

We consider a two-dimensional (2D) Chern insulator (CI) coupled to a conductor, and the line $x = 0$ separates them (see Fig. 1). The whole system is described by the Hamiltonian $\mathcal{H} = \mathcal{H}_{\text{TI}} + \mathcal{H}_{\text{cond}} + \mathcal{W}$ with hermiticity $\mathcal{H} = \mathcal{H}^\dagger$.

$$\mathcal{H}_{\text{TI}} = t_1 \sum_{\langle i,j \rangle} c_i^\dagger c_j + it_2 \sum_{\langle\langle i,j \rangle\rangle} v_{ij} c_i^\dagger c_j \quad (1)$$

is the Hamiltonian of the Haldane model without breaking the inversion symmetry; t_1 and t_2 are the nearest and next-nearest neighbor hopping of the honeycomb lattice (let's denote the sublattice as A and B); $v_{ij} = \pm 1$ depending on the vectors along the two bonds. By referring to the phase diagram of the Haldane model, one can find \mathcal{H}_{TI} is in the topological phase and the two bands are separated by $\mathbb{G} \equiv (-3\sqrt{3}t_2, 3\sqrt{3}t_2)$, indicating the topological states in the gap. For simplicity, we take the conductor on a square lattice, with its sites near the junction only connecting to the sublattice; the type of lattice or connections, in general, does not affect our conclusion. The Hamiltonian

$$\mathcal{H}_{\text{cond}} = \lambda_1 \sum_{\langle i,j \rangle_x} a_i^\dagger a_j + \lambda_2 \sum_{\langle i,j \rangle_y} a_i^\dagger a_j + \mu \sum_i a_i^\dagger a_i \quad (2)$$

describes the conductor with its band spanning $\mathbb{B} \equiv [u - 2|\lambda_1| - 2|\lambda_2|, u + 2|\lambda_1| + 2|\lambda_2|]$. μ denotes the onsite energy and λ_1 or λ_2 is the nearest neighbor hopping along x or y of the square lattice. $\mathcal{H}_{\text{cond}}$ is topologically trivial since it has only one band and the total Chern number must be zero.

$$\mathcal{W} = \lambda_1 \sum_{\langle i,j \rangle_x} a_i^\dagger c_j + h.c. \quad (3)$$

gives the coupling between \mathcal{H}_{TI} and $\mathcal{H}_{\text{cond}}$.

Several cases are rather trivial or well-studied and hence been excluded here: (i) the excitation energy ε is in the conduction bands of CI and the conductor, the transport perpendicular to the interface is much like that between conductors; (ii) the excitation energy is in the conduction band of CI and the band gap of the conductor, the perpendicular transport is blocked; (iii) the energy is in their gaps, it is well known that the transport along the interface is unidirectional and the number of the channel equals the Chern number [25, 26]. Instead, we consider the transport parallel to the interface when $\varepsilon \in \mathbb{B} \cap \mathbb{G}$. In that case, \mathcal{H}_{TI} can be reduced to the effective Hamiltonian H_{edge} for the edge states, and the reservoir assumption leads to that the effect of $\mathcal{H}_{\text{cond}}$ and \mathcal{W} can be replaced by the self-energy Σ of the conductors [27, 28]. That is

$$\mathcal{H} \rightarrow H_{\text{eff}} = H_{\text{edge}} + \Sigma = \frac{t_1}{2} \begin{pmatrix} \sin \frac{k_y}{2} \\ \frac{1}{2}(1 - e^{-ik_y}) \end{pmatrix} - \frac{1}{2} \begin{pmatrix} \Lambda + \sqrt{-4\lambda_1^2 + \Lambda^2} \\ 0 \end{pmatrix}. \quad (4)$$

where $\Lambda = \mu - \varepsilon + 2\lambda_2 \cos k_y$. Here, we represent reduced H_{eff} in k_y -momentum space by noticing the translation symmetry along y -axis. In section II of supplementary material (SM), we show that the Haldane model is exactly solvable through Green's function technique, and H_{edge} is constructed out of the edge state projector. Note that an extra eigenstate whose eigenvalue is zero appears in constructing H_{eff} , and we need to drop it in the calculation. Also in there, Σ is calculated with the help of the transfer matrix.

$H_{\text{edge}} = H_{\text{edge}}^\dagger$ but $\Sigma \neq \Sigma^\dagger$ if $\varepsilon \in \mathbb{B}$ hence the effective Hamiltonian H_{eff} of the interface is NH even though the whole system \mathcal{H} is *Hermitian*. Corresponding to excluded case (iii) mentioned above, $\Sigma = \Sigma^\dagger$ and $\Sigma \neq 0$ if $\varepsilon \notin \mathbb{B}$, Σ will renormalize the edge state, and the dashed line in Fig. 2b represents the renormalized response profile of the edge state concerning the excitation. Clearly, the wave propagation along the interface is lossless and unidirectional. We remark that the non-Hermiticity lies in the reservoir assumption, which can be roughly understood as that the conductor is significantly larger than the topological insulator, and this assumption fails when considering two comparable subsystems.

It is very hard to find a tight-binding chain lattice that corresponds to H_{eff} , so to give it an intuition, we consider the approximation model (e.g., $\sin \frac{k_y}{2} \approx \frac{1}{2} \sin k_y$) around $k_y = 0$ and set $\lambda_1 = t_1 = 1$, $\lambda_2 = -0.9$ and $\mu = \varepsilon = 0$. Correspondingly, the element in the first row and first column of H_{eff} :

$$[H_{\text{eff}}]_{11} = 2\xi \sin k_y + 2\gamma \cos k_y - 1.56i, \quad (5)$$

where $2\xi = 0.25$ and $2\gamma = 0.9 + 1.13i$. Figure 2a depicts the approximation tight-binding chain. The last term in the equation manifests as a global dissipation, while the rest of $[H_{\text{eff}}]_{11}$ is nothing but the Hatano-Nelson model [29] describing the vortex pinning in superconductors. The hopping in this model is asymmetric, i.e. $t_{ij} = -i\xi + \gamma$ from site j to i while $t_{ji} = i\xi + \gamma$ from site i to j , and $t_{ij} \neq t_{ji}^*$; it follows that the bulk states pile up at the boundary, namely, the NH skin effect. To describe the dispersion relation correctly, one needs to generalize $k_y \in \mathbb{R}$ to the complex domain $k_y \in \mathbb{C}$ [7, 30], and this can lead to non-bloch transport [31].

The response profile $|\varphi|$ at the interface corresponding to an excitation is an indicator of the non-Bloch transport due to $k_y \in \mathbb{C}$. In the NH Bloch case where $E \in \mathbb{C}$

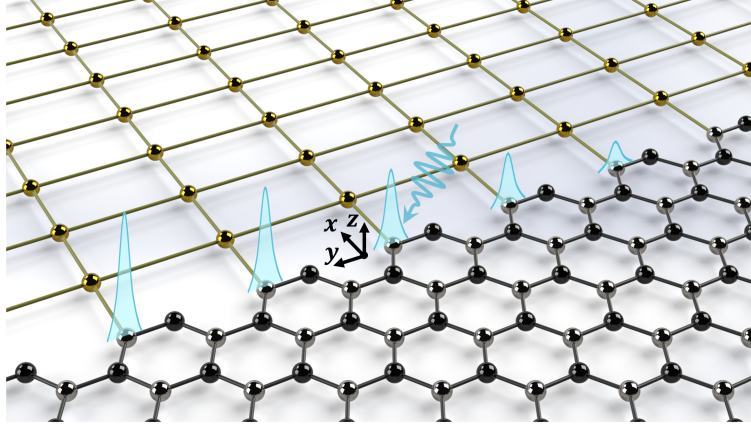


FIG. 1. Junction between the topological insulator (Haldane model) and the conductor. The next-nearest neighbor hopping t_2 is not plotted for simplicity.

and $k_y \in \mathbb{R}$, the profile $|\varphi| \propto \begin{cases} e^{\beta y}, & y < 0 \\ e^{-\beta y}, & y > 0 \end{cases}, \beta \in \mathbb{R}$ due to the global dissipation (let the excitation at $y = 0$). This means that the wave transport will decay at the same rate away from the excitation. When $E \in \mathbb{R}$ and $k_y \in \mathbb{C}$, the standard non-Bloch case, $|\varphi| \propto e^{\alpha y}, \alpha \in \mathbb{R}$. Consequently, the transport is amplified in one direction but is attenuated in the opposite. In general, the superposition of different transport types leads to $|\varphi| \sim \begin{cases} e^{(\alpha+\beta)y}, & y < 0 \\ e^{(\alpha-\beta)y}, & y > 0 \end{cases}$ (more statements see section IV of SM). So, the different decay (or growth) rates away from the excitation in the opposite direction indicate the non-Bloch transport. It is worth mentioning that analyzing the response profile in non-Bloch problems is more practical, as it can be directly accessible through regular scattering measurements.

Figure 2b (black solid line) shows the response profile along the interface from simulation, which corresponds to the general case where $E, k_y \in \mathbb{C}$. Clearly, it is non-Bloch transport even though the entire system is Hermitian. Moreover, in order to compensate for the global dissipation we apply onsite gain to the interface in another simulation, and we have the standard non-Bloch transport (see red line in Fig. 2b) corresponding to the case where $E \in \mathbb{R}$ and $k_y \in \mathbb{C}$.

The non-Bloch wave at the TI-conductor junction is universal. The reason is two-fold: (i) as part of the junction, the TI does not have to be the type of CI. The localized edge states make it possible to construct an effective one-dimensional system through the interface of two-dimensional materials. So, in principle, the CI (class A) used here can be replaced by other types of TI (e.g. class AII). In a separate work [32], we realize the \mathbb{Z}_2 NH skin effect at the interface between a time-reversal TI and a conductor; (ii) in contrast to Ref. [33], no extra requirement for the conductor is adopted here. In there, a relative momentum shift between the reservoir and the nanowire leads to asymmetric hopping. However, this

asymmetry in our model results from the interaction between the unidirectional topological states and the reservoir self-energy.

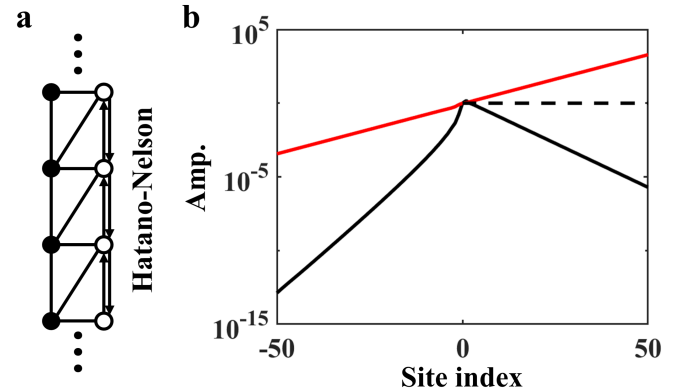


FIG. 2. Effective model and response profile. (a) Effective chain model at the junction around $k_y = 0$. One of the sub-chain is the Hatano-Nelson model. (b) The response profile (from Kwant simulation [34]) at the interface when an excitation is injected at the origin. Note that logarithmic scale is on the vertical axis. Dashed line: profile of the one-way topological state of the Haldane model. Black solid line: profile at the interface, and the different decay rates (left: 1.7, right: 0.3) away from the excitation in the opposite direction suggest the non-Bloch transport. Red solid line: profile when the onsite gain is added on sublattice A.

III. EXPERIMENTAL DEMONSTRATION

Circuit.—Implementing temporal topoelectrical circuit (TTC) [31, 35] theory, we can construct a circuit lattice with those correspondences, Hamiltonian $\mathcal{H} \leftrightarrow$ admittance Y of circuits, eigenvalues of $\mathcal{H} \leftrightarrow$ self-admittance Y_0 of circuits, and eigenmodes of $\mathcal{H} \leftrightarrow$ voltage on the circuit nodes. Figure 3a illustrates the schematic of the

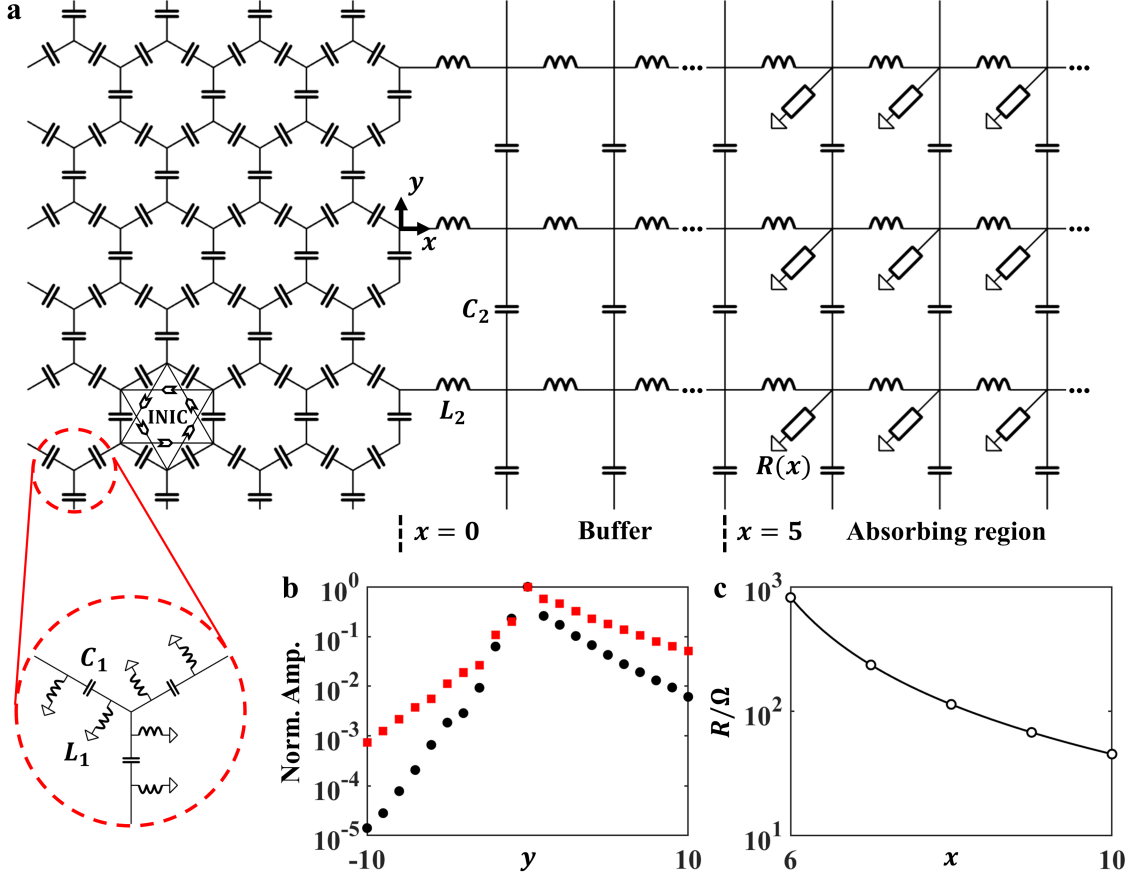


FIG. 3. Experimental demonstration. (a) Circuit schematics. The INIC is used to realize the next-neighbor hopping (only a few instances are illustrated). The inset shows the grounding configuration, which ensures equal self-admittance for each node of the honeycomb lattice. Note that one connecting capacitor $C_1 = 1$ nF along with two grounding inductors $L_1 = 3.3$ μ H between every two adjacent nodes forms a Π -shaped circuit. $C_2 = 100$ pF and $L_2 = 3.3$ μ H. (b) Experimental results of the profile (black dots), indicating the non-Bloch transport. Red squares are the results from CST microwave field-circuit co-simulation of reverse design. (c) The grounding resistance $R(x)$ varies as x . In absorbing region, the complex potentials are realized by grounding all nodes with resistances.

designed circuit lattice and Fig. 3b (black dots) shows the voltage response profile under a current excitation from the experiment. Without the square lattice, which acts as the conductor $\mathcal{H}_{\text{cond}}$, the voltage propagates in a unidirectional manner. However, when it is introduced, the voltage wave propagates in both directions but with different decay rates, indicating the non-Bloch transport. In the experiment, the time-reversal-breaking term t_2 is realized by the negative impedance converter with current inversion (INIC, Fig. 3a).

In the model of \mathcal{H} , we assume that the size of the conductor $\mathcal{H}_{\text{cond}}$ is semi-infinite such that it serves as a reservoir. It is very cumbersome to prepare the circuit sample in that size. Instead, one can reduce the semi-infinite geometry to a finite lattice with proper boundary condition, i.e., the perfect absorbing boundary condition using power-growth complex onsite potentials that completely absorb the incident wave. That gradient complex potentials are realized by grounding the nodes with resistances (see Fig. 3c). More circuit experiments refer to

section VIII of SM. We remark that the boundary complex potential is not the origin of non-Bloch transport and the semi-infinite argument may also be mitigated by a fairly large lattice.

Electromagnetic metamaterials.—The normal design of topological metamaterials costs substantial computational resources: start with geometry and material parameters; then calculate the band structure by finite element simulation; if the band is not topological, tune the parameter and start over. On the contrary, the proposed reverse design is non-iterative and in principle requires minimal computational resources: it starts with a tight-binding model, then designs a circuit network based on the TTC, and finally generalizes the network to the electromagnetic/optical metamaterials. As a proof of concept, we illustrate this idea by realizing the junction mentioned above in the S band (2 – 4 GHz) range, and the design scheme is readily generalized to the optical range.

It takes two steps to generalize the lumped circuit network mentioned above to electromagnetic/optical meta-

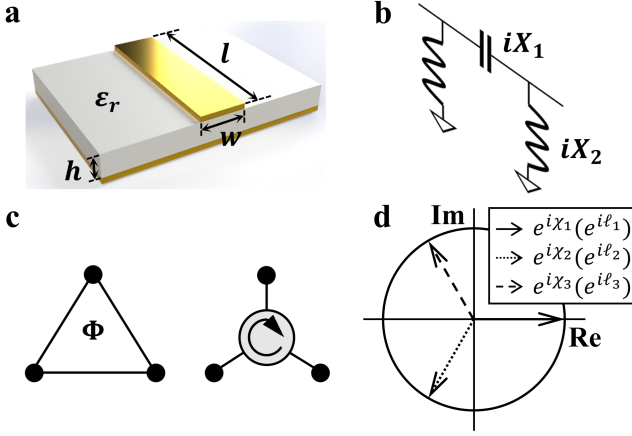


FIG. 4. Principle of the reverse design and introducing non-reciprocal hopping t_2 . (a) Schematic diagram of microstrip waveguide. $w = 2.2$ mm, $h = 1.2$ mm and $\epsilon_r = 4.6$ lead to the characteristic impedance $Z_0 = 50 \Omega$ at 2.4 GHz. (b) Π -shape equivalent lumped circuit model of the microstrip. (c) Equivalent connectivity between the Δ -configuration of the three-site model and the Y-configuration of a circulator, and their characteristics (d) when $\Phi = 3\pi/2$. $\chi_i \leftrightarrow \ell_i$ uniquely specify the hopping relation between the three sites.

materials. This is because INIC that breaks time-reversal symmetry does not have a counterpart in that frequency range, step two will handle that. We remark that compared to the existing topoelectrical circuits [36–38], TTC is more suitable to be the starting point of the reverse design, because the impedance measurements required by existing circuits are out of reach in scattering experiments while scattering measurements are more accessible for electromagnetic metamaterials.

First, consider the circuit network without INIC. The key observation is that each Π -shape circuit in the network is equivalent to a segment of waveguide with electrical length kl , where k is wavenumber in the waveguide and l is the physical length. The admittances of the grounding inductors and the connecting capacitor are

$$iX_1 = -i \frac{1}{Z_0 \sin kl}, \quad iX_2 = i \frac{1}{Z_0} \tan \frac{kl}{2}, \quad (6)$$

respectively, where Z_0 is the characteristic impedance of the waveguide. One can easily check this equivalence by calculating the two-port scattering matrix of the Π -shape circuit (Fig. 4b) and the waveguide [39]. Here, we choose the waveguide as the microstrip line (Fig. 4a). In the honeycomb lattice, we set $kl = 3\pi/2$, which corresponds to $C = 1.3$ pF and $L = 3.3$ nH at 2.4 GHz. In the square lattice we set $kl = 3\pi/2$ for λ_1 and $kl = 9\pi/2$ for λ_2 , which also corresponds to $C = 1.3$ pF and $L = 3.3$ nH at 2.4 GHz, with grounding and connecting components exchanged. Note that the values of lumped elements should be scaled up/down owing to the frequency change.

Next, we show how to introduce the next neighbor T-breaking hopping t_2 of \mathcal{H}_{TI} which is critical to the Haldane model. It is well-known this T-breaking term can

be realized by nonreciprocal devices [40–43], e.g., a RF circulator. In reality, a nonreciprocal device has very limited bandwidth, for example, the typical bandwidth is a few hundreds MHz for a RF circulator working at GHz, thus the frequency range of resonance-based metamaterials emulating the tight-binding Haldane model should be in this bandwidth. This frequency concern should not bother us since our TTC or TTC-based design operates at a fixed frequency and is not resonance-based. According to our previous works [31, 35], it looks like introducing the hopping t_2 can be easily achieved by finding out the admittance of the RF circulator, however, in general, the circulator does not have a well-defined admittance (Part A in section V of SM).

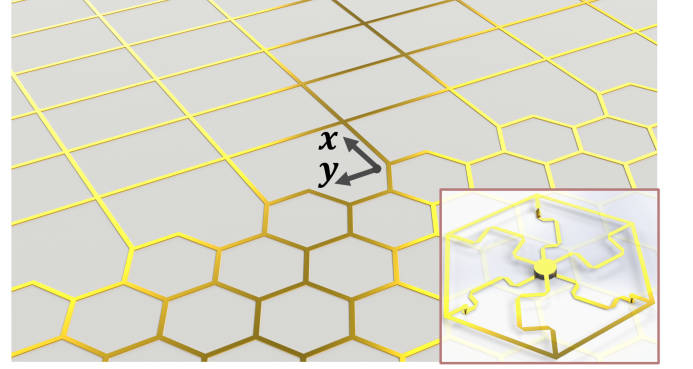


FIG. 5. Metamaterial realization of non-Bloch transport under reverse design. Metamaterial junction consists of microstrip lines. For clarity, three-port circulators and their connecting lines that lead to the non-reciprocal coupling t_2 are only shown in the inset, where substrates and the middle layer of ground plane are not plotted. The perfect match layer (PML) boundary condition is applied to mimic the semi-infinite conductor.

To solve that, let's first understand the hopping in a geometric manner. Without loss of generality, we consider a minimal model containing three identical sites with hopping t_2 connecting them. The flux Φ in the plaquette leads to a phase $\theta = \frac{\Phi}{3}$ in t_2 , and the Hamiltonian is

$$\mathcal{H}_{\Delta}/t_2 = (\Lambda_1 + \Lambda_4 + \Lambda_6) \cos \theta + (\Lambda_2 - \Lambda_5 + \Lambda_7) \sin \theta \quad (7)$$

where Λ_i are the Gell-Mann matrices. When $\Phi = 0$, \mathcal{H}_{Δ} respects D3h symmetry, thus it has two-fold degeneracy eigenvalues. When pumping the flux, the symmetry is lifted down to C3, resulting in the splitting of the degeneracy (note that when $\Phi = n\pi$ with $n \in \mathbb{Z}$, \mathcal{H}_{Δ} respects D3h up to a gauge). So, we can use the frame of $\mathbf{u} = (\mathbf{v}_1, \mathbf{v}_2, \mathbf{v}_3)$, $\mathbf{v}_1 = (1, 1, 1)^T$, $\mathbf{v}_2 = (1, \alpha, \alpha^2)^T$, $\mathbf{v}_3 = (1, \alpha^2, \alpha)^T$ with $\alpha = e^{\frac{2\pi i}{3}}$. Performing a bilinear transform, we have

$$\mathcal{S} = \frac{i + \mathcal{H}_{\Delta}}{i - \mathcal{H}_{\Delta}}. \quad (8)$$

\mathcal{S} is unitary: $\mathcal{S}\mathcal{S}^\dagger = 1$, and in the frame of \mathbf{u} : $\mathbf{u}^{-1}\mathcal{S}\mathbf{u} = \text{diag}(e^{i\chi_1}, e^{i\chi_2}, e^{i\chi_3})$. So, characteristics $\chi_{1,2,3}$ uniquely

specify the hopping relation between the sites (see Fig. 4d). On the other hand, compared to the admittance, the scattering-parameter of a circulator is always well-defined. In section V of SM, we demonstrate that three similar characteristics (ℓ_1, ℓ_2, ℓ_3) in a circulator uniquely determine the connectivity of the three sites; this gives us an correspondence of T-breaking hopping between tight-binding models and the metamaterials (Fig. 4c): $\chi_i \leftrightarrow \ell_i$. In section VI of SM, the simulation establishes that the topological metamaterial designed under this correspondence supports the unidirectional edge state just as the Haldane model does.

Figure 5 shows the final RF design of the junction with microstrip lines, and Fig. 3b (red squares) gives the electric field profile with respect to an excitation (from CST field-circuit co-simulation). Clearly, the metamaterial junction exhibits the property of the non-Bloch transport, which is consistent with the prediction.

IV. OUTLOOKS

In summary, we provide an alternate approach to realize non-Hermitian systems in electromagnetics in a gain/loss-free fashion. The reverse design procedure, i.e., the tight-binding models \rightarrow temporal topoelectrical circuits \rightarrow electromagnetic metamaterials, offers a prevalent paradigm to design the topological band of the metamaterials.

ACKNOWLEDGMENTS

We gratefully acknowledge the insights of and discussions with Fuxin Guan, Bo Zhen, Ce Shang, Qinghua Song and Li Ge.

This work was supported by National Key Research & Development Program of China (Grant No. 2023YFB3811400) and National Natural Science Foundation of China (Grant No. 52273296).

-
- [1] M.-A. Miri and A. Alu, Exceptional points in optics and photonics, *Science* **363**, eaar7709 (2019).
 - [2] C. M. Bender, Making sense of non-hermitian hamiltonians, *Reports on Progress in Physics* **70**, 947 (2007).
 - [3] A. Mostafazadeh, Pseudo-Hermiticity versus PT symmetry: The necessary condition for the reality of the spectrum of a non-Hermitian Hamiltonian, *Journal of Mathematical Physics* **43**, 205 (2002).
 - [4] E. J. Bergholtz, J. C. Budich, and F. K. Kunst, Exceptional topology of non-hermitian systems, *Rev. Mod. Phys.* **93**, 015005 (2021).
 - [5] T. Dai, Y. Ao, J. Mao, Y. Yang, Y. Zheng, C. Zhai, Y. Li, J. Yuan, B. Tang, Z. Li, *et al.*, Non-hermitian topological phase transitions controlled by nonlinearity, *Nature Physics* **20**, 101 (2024).
 - [6] J. Hu, R.-Y. Zhang, Y. Wang, X. Ouyang, Y. Zhu, H. Jia, and C. T. Chan, Non-hermitian swallowtail catastrophe revealing transitions among diverse topological singularities, *Nature Physics* **19**, 1098 (2023).
 - [7] S. Yao and Z. Wang, Edge states and topological invariants of non-hermitian systems, *Phys. Rev. Lett.* **121**, 086803 (2018).
 - [8] F. K. Kunst, E. Edvardsson, J. C. Budich, and E. J. Bergholtz, Biorthogonal bulk-boundary correspondence in non-hermitian systems, *Phys. Rev. Lett.* **121**, 026808 (2018).
 - [9] K. Zhang, Z. Yang, and C. Fang, Correspondence between winding numbers and skin modes in non-hermitian systems, *Phys. Rev. Lett.* **125**, 126402 (2020).
 - [10] T. Helbig, T. Hofmann, S. Imhof, M. Abdelghany, T. Kiessling, L. W. Molenkamp, C. H. Lee, A. Szameit, M. Greiter, and R. Thomale, Generalized bulk-boundary correspondence in non-hermitian topoelectrical circuits, *Nature Physics* **16**, 10.1038/s41567-020-0922-9 (2020).
 - [11] K. Ochkan, R. Chaturvedi, V. Könye, L. Veyrat, R. Giraud, D. Mailly, A. Cavanna, U. Gennser, E. M. Hankiewicz, B. Büchner, *et al.*, Non-hermitian topology in a multi-terminal quantum hall device, *Nature Physics* **20**, 395 (2024).
 - [12] L. Feng, R. El-Ganainy, and L. Ge, Non-hermitian photonics based on parity-time symmetry, *Nature Photonics* **11**, 752 (2017).
 - [13] R. El-Ganainy, K. G. Makris, M. Khajavikhan, Z. H. Musslimani, S. Rotter, and D. N. Christodoulides, Non-hermitian physics and pt symmetry, *Nature Physics* **14**, 11 (2018).
 - [14] V. V. Konotop, J. Yang, and D. A. Zezyulin, Nonlinear waves in \mathcal{PT} -symmetric systems, *Rev. Mod. Phys.* **88**, 035002 (2016).
 - [15] T. Ozawa, H. M. Price, A. Amo, N. Goldman, M. Hafezi, L. Lu, M. C. Rechtsman, D. Schuster, J. Simon, O. Zilberberg, and I. Carusotto, Topological photonics, *Rev. Mod. Phys.* **91**, 015006 (2019).
 - [16] X. Feng, T. Wu, Z. Gao, H. Zhao, S. Wu, Y. Zhang, L. Ge, and L. Feng, Non-hermitian hybrid silicon photonic switching, *Nature Photonics*, 1 (2025).
 - [17] Z. Rao, C. Meng, Y. Han, L. Zhu, K. Ding, and Z. An, Braiding reflectionless states in non-hermitian magnonics, *Nature Physics*, 1 (2024).
 - [18] C. E. Rüter, K. G. Makris, R. El-Ganainy, D. N. Christodoulides, M. Segev, and D. Kip, Observation of parity-time symmetry in optics, *Nature Physics* **6**, 192 (2010).
 - [19] R. El-Ganainy, K. G. Makris, D. N. Christodoulides, and Z. H. Musslimani, Theory of coupled optical pt-symmetric structures, *Opt. Lett.* **32**, 2632 (2007).
 - [20] B. Zhen, C. W. Hsu, Y. Igarashi, L. Lu, I. Kaminer, A. Pick, S.-L. Chua, J. D. Joannopoulos, and M. Soljačić, Spawning rings of exceptional points out of dirac cones, *Nature* **525**, 354 (2015).
 - [21] H. Li, A. Mekawy, A. Krasnok, and A. Alù, Virtual parity-time symmetry, *Phys. Rev. Lett.* **124**, 193901 (2020).

- [22] F. Guan, X. Guo, K. Zeng, S. Zhang, Z. Nie, S. Ma, Q. Dai, J. Pendry, X. Zhang, and S. Zhang, Overcoming losses in superlenses with synthetic waves of complex frequency, *Science* **381**, 766 (2023).
- [23] S. Kim, A. Krasnok, and A. Alù, Complex-frequency excitations in photonics and wave physics, *Science* **387**, eado4128 (2025).
- [24] A. Roy, S. Jahani, Q. Guo, A. Dutt, S. Fan, M.-A. Miri, and A. Marandi, Nondissipative non-hermitian dynamics and exceptional points in coupled optical parametric oscillators, *Optica* **8**, 415 (2021).
- [25] M. Z. Hasan and C. L. Kane, Colloquium: Topological insulators, *Rev. Mod. Phys.* **82**, 3045 (2010).
- [26] X.-L. Qi and S.-C. Zhang, Topological insulators and superconductors, *Rev. Mod. Phys.* **83**, 1057 (2011).
- [27] S. Datta, *Electronic transport in mesoscopic systems* (Cambridge university press, 1997).
- [28] E. J. Bergholtz and J. C. Budich, Non-hermitian weyl physics in topological insulator ferromagnet junctions, *Phys. Rev. Res.* **1**, 012003 (2019).
- [29] N. Hatano and D. R. Nelson, Localization transitions in non-hermitian quantum mechanics, *Phys. Rev. Lett.* **77**, 570 (1996).
- [30] K. Yokomizo and S. Murakami, Non-bloch band theory of non-hermitian systems, *Phys. Rev. Lett.* **123**, 066404 (2019).
- [31] M. Wu, Q. Zhao, L. Kang, M. Weng, Z. Chi, R. Peng, J. Liu, D. H. Werner, Y. Meng, and J. Zhou, Evidencing non-bloch dynamics in temporal topoelectrical circuits, *Phys. Rev. B* **107**, 064307 (2023).
- [32] In preparation, .
- [33] H. Geng, J. Y. Wei, M. H. Zou, L. Sheng, W. Chen, and D. Y. Xing, Nonreciprocal charge and spin transport induced by non-hermitian skin effect in mesoscopic heterojunctions, *Phys. Rev. B* **107**, 035306 (2023).
- [34] C. W. Groth, M. Wimmer, A. R. Akhmerov, and X. Waintal, Kwant: a software package for quantum transport, *New Journal of Physics* **16**, 063065 (2014).
- [35] M. Wu, M. Weng, Z. Chi, Y. Qi, H. Li, Q. Zhao, Y. Meng, and J. Zhou, Observing relative homotopic degeneracy conversions with circuit metamaterials, *Phys. Rev. Lett.* **132**, 016605 (2024).
- [36] C. H. Lee, S. Imhof, C. Berger, F. Bayer, J. Brehm, L. W. Molenkamp, T. Kiessling, and R. Thomale, Topoelectrical circuits, *Communications Physics* **1**, 39 (2018).
- [37] S. Imhof, C. Berger, F. Bayer, J. Brehm, L. W. Molenkamp, T. Kiessling, F. Schindler, C. H. Lee, M. Greiter, T. Neupert, and R. Thomale, Topoelectrical-circuit realization of topological corner modes, *Nature Physics* **14**, 925 (2018).
- [38] C. Shang, S. Liu, R. Shao, P. Han, X. Zang, X. Zhang, K. N. Salama, W. Gao, C. H. Lee, R. Thomale, A. Manchon, S. Zhang, T. J. Cui, and U. Schwingenschlogl, Experimental identification of the second-order non-hermitian skin effect with physics-graph-informed machine learning, *Advanced Science* **9**, 10.1002/adv.202202922 (2022).
- [39] N. Marcuvitz, *Waveguide handbook* (Institution of Electrical Engineers, GBR, 1986).
- [40] Z. Wang, Y. Chong, J. D. Joannopoulos, and M. Soljačić, Observation of unidirectional backscattering-immune topological electromagnetic states, *Nature* **461**, 772 (2009).
- [41] Z. Yang, F. Gao, X. Shi, X. Lin, Z. Gao, Y. Chong, and B. Zhang, Topological acoustics, *Phys. Rev. Lett.* **114**, 114301 (2015).
- [42] T. Hofmann, T. Helbig, C. H. Lee, M. Greiter, and R. Thomale, Chiral voltage propagation and calibration in a topoelectrical chern circuit, *Phys. Rev. Lett.* **122**, 247702 (2019).
- [43] Z. Zhang, P. Delplace, and R. Fleury, Superior robustness of anomalous non-reciprocal topological edge states, *Nature* **598**, 293 (2021).

Gain/Loss-free Non-Hermitian Metamaterials

Maopeng Wu,^{1,*} Mingze Weng,^{1,*} Zhonghai Chi,² Siyong Zheng,² Fubei Liu,² Weijia Luo,² Qian Zhao,^{1,†} Yonggang Meng,¹ and Ji Zhou^{2,‡}

¹*State Key Laboratory of Tribology in Advanced Equipment,
Department of Mechanical Engineering, Tsinghua University, Beijing 100084, China*

²*State Key Laboratory of New Ceramics and Fine Processing,
School of Materials Science and Engineering, Tsinghua University, Beijing 100084, China*

(Dated: April 21, 2025)

CONTENTS

I. A review about self-energy	1
A. Junction	1
B. Reservoir argument	1
II. Edge state Hamiltonian	2
A. Green's function with periodic boundaries	3
B. Hopping perturbation	3
C. Green's function with the perturbation	3
D. Edge state wave vector	4
III. Self-energy	4
IV. Response profile	5
V. Realization of the hopping with a phase	6
A. Ill-defined admittance of microwave circulators	6
B. Review of signal flow graphs	7
C. Two sites	8
D. Three sites	8
E. Four sites	9
VI. Simulations of microstrip line metamaterials	10
A. Upgrade of TTCs	10
B. ML Haldane model	11
C. Field-circuit co-simulation of the junction	12
VII. Kwant simulation	13
A. Topological junction	14
B. Imaginary absorbing potential	14
VIII. Experimental details	14
A. Circuit realization of Haldane model	15
B. Circuit realization of the semi-infinite conductor	15
C. Measuring of the non-Bloch transport	15
References	15

I. A REVIEW ABOUT SELF-ENERGY

A. Junction

Let us first give the topological junction an intuition. Assuming each side of the junction is described by a Hermitian Hamiltonian, H_0 and H_e , and the two sides are coupled through some surface mechanism, such as the chemical bonds. Then the junction is Hermitian and the total Hamiltonian can be written as.

$$H_J = \begin{pmatrix} H_0 & C \\ C^\dagger & H_e \end{pmatrix}, \quad (1)$$

where C denotes the coupling. Correspondingly, the retarded green function G_J can be defined as $G_J = (E + i0^+ - H_J)^{-1}$ or

$$G_J = \begin{pmatrix} G_0 & G_{0e} \\ G_{e0} & G_e \end{pmatrix}. \quad (2)$$

When one of the sides is so “large”, say the side described by H_e , that the effect of H_0 on H_e is negligible. In this case, H_e constitutes a reservoir or the environment. After some simple algebra, we can find the Green's function G_0 of the smaller side is expressed as $G_0 = E + i0^+ - H_0 - \Sigma$, where $\Sigma = C^\dagger G_e^{-1} C$ is the so called self-energy and the effect of H_e on H_0 is encoded with it. So the effective Hamiltonian H_{eff} of the smaller side is $H_{\text{eff}} = H_0 + \Sigma$, and in general H_{eff} is non-Hermitian $H_{\text{eff}} \neq H_{\text{eff}}^\dagger$ owing to the complexity of Σ . Note that the non-Hermiticity is introduced without any gain or loss, while the gain and loss are essential in optical realization. The concept of self-energy is widely applied in physics, such as those coming from the electron-electron/phonon Coulomb interactions, the impurity scattering and the interaction with the reservoir (considered here), although their physical origins may differ.

B. Reservoir argument

In the main article, we realize an effective NH system by considering two coupled subsystems. The self-energy treatment requires that one of the subsystems can be viewed as the reservoir. Here we show that self-energy is out of the capability to delineate two comparable coupled subsystems.

* These two authors contributed equally.

† zhaoqian@tsinghua.edu.cn

‡ zhouji@tsinghua.edu.cn

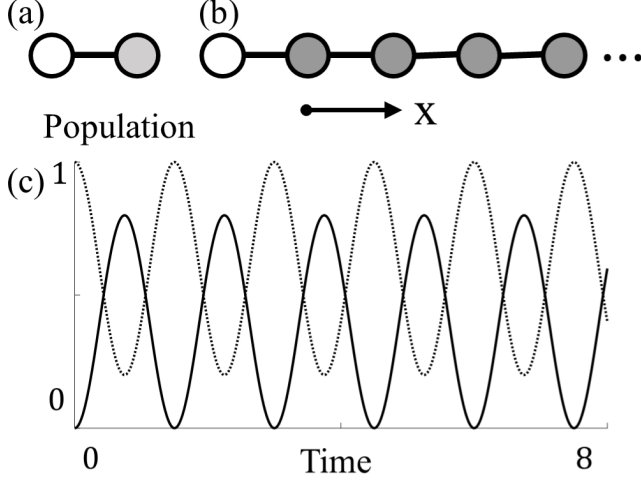


FIG. 1. Reservoir argument. (a) Two comparable coupled subsystems I and II. (b) Two coupled subsystems with the subsystem II consisting of N states. (c) The population dynamics as a function of time in two comparable coupled subsystems. $E_1 = 0$, $E_2 = 1$ and $\Omega = 1$. The solid line represents ρ_{11} and the dot line represents ρ_{22} , the populations present Rabi oscillations.

Let's consider two comparable coupled subsystems with only one state in each (Fig. 1a). The whole system is described by

$$\mathcal{H}_2 = E_1 a^\dagger a + E_2 b^\dagger b + \Omega(a^\dagger b + b^\dagger a), \quad (3)$$

a^\dagger and a are creation and annihilation operator in subsystem I respectively, b^\dagger and b in subsystem II. Now if we are interested primarily in I, the effect of II through a self-energy is

$$\Sigma_2(\varepsilon) = \frac{\Omega}{\varepsilon - E_1 + i0^+}. \quad (4)$$

However, II is not a reservoir in the common sense. The fundamental feature of a reservoir is that the rate constant for outflow or inflow (e.g., heat flow, current flow) remains unaffected by the filling and vacuuming of states and other dynamical details [1]. II does not satisfy this criterion because the escape rate is

$$\gamma_2 = i(\Sigma_2 - \Sigma_2^\dagger) = \frac{\Omega^2 0^+}{(\varepsilon - E_1)^2 + (0^+)^2} \quad (5)$$

which is affected strongly by 0^+ (a proper reservoir should be independent of 0^+). This means that rate out of I is affected by the rate into it. By using the von-Neumann equation $\frac{d\rho}{dt} = -i[\mathcal{H}_2, \rho]$ we could calculate the populations (ρ_{11}, ρ_{22}) of density matrix ρ as a function of time. The system is then driven between subsystems, and the populations present Rabi oscillations with frequency Ω , as is shown in Fig. 1c.

Now consider two coupled subsystems with the subsystem II consisting of N states (e.g., a chain with N sites,

see Fig. 1b), the resulting Hamiltonian is

$$\mathcal{H}_{N+1} = E_1 a^\dagger a + E_2 \sum_i b_i^\dagger b_i + \left[t \sum_i b_i^\dagger b_{i+1} + \Omega a^\dagger b_1 + h.c. \right]. \quad (6)$$

The eigenenergies of II are given by $\varepsilon_n = E_2 + 2t \cos k_n$ and the corresponding normalized wavefunction is $\phi = \sqrt{\frac{2}{N}} \sin k_n x$, where $k_n = n \frac{\pi}{N}$, $n \in \mathbb{Z}$. So, the effect of II through the self-energy is

$$\Sigma_{N+1}(\varepsilon) = \frac{2}{N} \sum_n \frac{\Omega^2 \sin^2 k_n}{\varepsilon - \varepsilon_n + i0^+}. \quad (7)$$

When $N \rightarrow \infty$, convert the summation to an integral:

$$\Sigma_\infty = \frac{2}{\pi} \int_0^\pi dk \frac{\Omega^2 \sin^2 k_n}{\varepsilon - \varepsilon_n + i0^+}, \quad (8)$$

and we have $\Sigma_\infty = \Omega e^{ik}$ (we set $E_1 = E_2$ for simplicity). The escape rate is $\gamma_\infty = i(\Sigma_\infty - \Sigma_\infty^\dagger) = 2\Omega \sin k$. By contrast, the reservoir II with $N \rightarrow \infty$ states has a constant escape rate independent of 0^+ .

II. EDGE STATE HAMILTONIAN

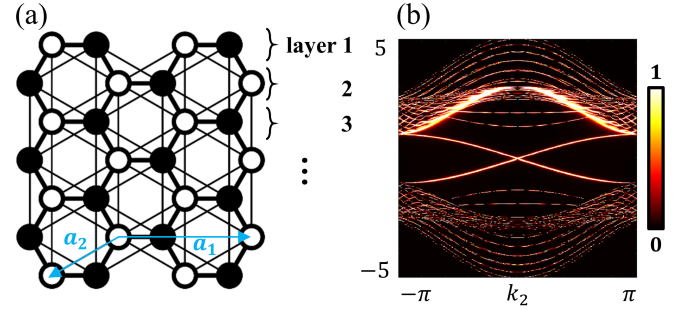


FIG. 2. (a) A semi-infinite two-dimensional honeycomb lattice and a chain of layers. a_1 and a_2 are the lattice unit vectors. We use the non-orthogonal coordinate based on a_1 and a_2 , and reciprocal space (k_1, k_2) corresponds to that coordinate. (b) Local density of states of $G(\varepsilon; k_1, l)$.

There are several ways to calculate the exact solutions of the edge states, such as via extending Bloch's theorem [2–4], the impurity Green's function [5, 6], the transfer matrix [7, 8], the geometric algebra [9] and so on. The difficulty for the Haldane model roots in the next-nearest neighbor hopping. Here, we follow the approach using the Green's function [9]. The calculation is summarized as follows: we begin with a model $h_0(\mathbf{k})$ with fully periodic boundary conditions, which allows us to write down the Hamiltonian in the momentum space; next, we add hopping perturbation $h_1(k_1)$ that substrate the interaction crossing the first row and the end row of the lattice, forming an open boundary along that direction; the final

Green's function of the resulting system $h_0 + h_1$ is given by the Dyson equation, and the poles of it enable the analytic solution of the edge states. Note that the geometric algebra method can not be applied here since the next-nearest neighbor hopping appears and the supercell Hamiltonian (e.g., two unit cells) is not of Dirac form.

A. Green's function with periodic boundaries

After Fourier transform, the Haldane model of Eq. 1 in the main text ($t_1 = 1$, Fig. 2a) can be expressed in a compact form as $h_0(\mathbf{k}) = \mathbf{d} \cdot \boldsymbol{\sigma}$, where

$$\begin{aligned} d_x &= 2t_2 [\sin k_2 + \sin(k_1 + k_2) - \sin(k_1 + 2k_2)], \\ d_y &= 1 + \cos k_2 + \cos(k_1 + k_2), \\ d_z &= -\sin k_2 + \sin(k_1 + k_2). \end{aligned} \quad (9)$$

And the spectrum of the model is $\varepsilon_{\mathbf{k}} = \pm \sqrt{d_x^2 + d_y^2 + d_z^2}$. Correspondingly, the Green function in \mathbf{k} space is

$$G_0(E; \mathbf{k}) = \frac{1}{\varepsilon - h_0(\mathbf{k})} = \frac{1}{\varepsilon^2 - \varepsilon_{\mathbf{k}}^2} \begin{pmatrix} \varepsilon + d_z & d_x - id_y \\ d_x + id_y & \varepsilon - d_z \end{pmatrix} \quad (10)$$

To include the hopping perturbation, we keep the momentum coordinate k_1 but perform an inverse Fourier transform to write down the Green's function in real-space coordinate in the a_2 direction. Thus, we have

$$G_0(E; k_1, l) = \begin{pmatrix} g_0 & g_1^\dagger & g_2^\dagger & \cdots & g_2 & g_1 \\ g_1 & g_0 & g_1^\dagger & g_2^\dagger & & g_2 \\ g_2 & g_1 & g_0 & g_1^\dagger & & \\ \vdots & g_2 & g_1 & g_0 & & \\ g_2^\dagger & & & & & \\ g_1^\dagger & g_2^\dagger & & & \ddots & \end{pmatrix}_{n,n} \quad (11)$$

where

$$\begin{aligned} g_0 &= \int \frac{dk_2}{2\pi} G_0(\varepsilon, \mathbf{k}), \\ g_1 &= \int \frac{dk_2}{2\pi} e^{ik_2} G_0(\varepsilon, \mathbf{k}), \\ g_2 &= \int \frac{dk_2}{2\pi} e^{2ik_2} G_0(\varepsilon, \mathbf{k}), \end{aligned} \quad (12)$$

and $l = ja_2$ with $j = 1, 2, \dots, n$. $G_0(\varepsilon; k_1, l)$ is a n -by- n block matrix.

B. Hopping perturbation

Hopping perturbation $h_1(\varepsilon; k_1, l)$ deletes the hopping crossing the first row and the end row of the lattice, such that it creates two edges perpendicular to a_1 . Its explicit expression is

$$h_1(\varepsilon; k_1, l) = \begin{pmatrix} 0 & \cdots & v_2 & v_1 \\ \vdots & & 0 & v_2 \\ v_2^\dagger & 0 & \ddots & \\ v_1^\dagger & v_2^\dagger & & 0 \end{pmatrix}_{n,n} \quad (13)$$

where

$$\begin{aligned} v_1 &= \begin{pmatrix} -it_2(1 + e^{ik_1}) & 1 \\ e^{ik_1} & it_2(1 + e^{ik_1}) \end{pmatrix}, \\ v_2 &= \begin{pmatrix} it_2e^{ik_1} & 0 \\ 0 & it_2e^{-ik_1} \end{pmatrix} \end{aligned} \quad (14)$$

$v_1(v_2)$ describes the nearest (next-nearest) neighbor hopping between the layers along a_2 .

C. Green's function with the perturbation

The Dyson equation gives the full Green's function $G(\varepsilon; k_1, l)$ in terms of the initial Green's function $G_0(\varepsilon; k_1, l)$ and the hopping perturbation h_1 , that is

$$G(\varepsilon; k_1, l) = \frac{G_0}{1 - G_0 h_1}. \quad (15)$$

The G_0 has no poles in the gap, so the poles of G , alternatively the zeros of $\det(1 - G_0 h_1)$, are the edge state eigenvalues when $\varepsilon \in \mathbb{G}$. To show that, we numerically calculate the local density of states given in general by $n(\varepsilon; k_1) = -\frac{1}{\pi} \text{Im}[\text{tr} G(\varepsilon; k_1, l)]$ (see Fig. 2b). Taking the ansatz of edge state wave vector $\phi = (u, \lambda u, \lambda^2 u, \dots, 0)_{1,n}^T$ and substituting 11 and 13 into 15, we have

$$(\mathbb{I} - G_0 h_1) \phi = \begin{pmatrix} I - \begin{pmatrix} g_2 & g_1 \\ g_3 & g_2 \end{pmatrix} \begin{pmatrix} v_2 & v_1 \\ 0 & v_2 \end{pmatrix}^\dagger & -\begin{pmatrix} g_0 & g_1^\dagger \\ g_1 & g_0 \end{pmatrix} \begin{pmatrix} v_2 & v_1 \\ 0 & v_2 \end{pmatrix} \\ \vdots & \vdots \\ -\begin{pmatrix} g_0 & g_1^\dagger \\ g_1 & g_0 \end{pmatrix} \begin{pmatrix} v_2 & v_1 \\ 0 & v_2 \end{pmatrix}^\dagger & I - \begin{pmatrix} g_2 & g_1 \\ g_3 & g_2 \end{pmatrix}^\dagger \begin{pmatrix} v_2 & v_1 \\ 0 & v_2 \end{pmatrix} \end{pmatrix} \begin{pmatrix} u \\ \lambda u \\ \vdots \\ 0 \end{pmatrix} \quad (16)$$

The ellipses indicate the non-zero subblock. ϕ localizes at the first layer and the $|\lambda| < 1$ promises the localization. And,

$$\begin{aligned} \left[I - \begin{pmatrix} g_2 & g_1 \\ g_3 & g_2 \end{pmatrix} \begin{pmatrix} v_2 & v_1 \\ 0 & v_2 \end{pmatrix}^\dagger \right] \begin{pmatrix} u \\ \lambda u \end{pmatrix} &= 0, \\ \begin{pmatrix} g_0 & g_1^\dagger \\ g_1 & g_0 \end{pmatrix} \begin{pmatrix} v_2 & v_1 \\ 0 & v_2 \end{pmatrix}^\dagger \begin{pmatrix} u \\ \lambda u \end{pmatrix} &= 0, \end{aligned} \quad (17)$$

which together require (Kramer criterion)

$$\det \begin{pmatrix} g_0 & g_1^\dagger \\ g_1 & g_0 \end{pmatrix} = 0. \quad (18)$$

It can be further simplified by a decomposition in terms of triangular matrices (note that $\det(g_0) \neq 0$),

$$\begin{aligned} \det \begin{pmatrix} g_0 & g_1^\dagger \\ g_1 & g_0 \end{pmatrix} &= \det \left[\begin{pmatrix} g_0 & 0 \\ g_1 & I \end{pmatrix} \begin{pmatrix} I & g_0^{-1} g_1^\dagger \\ 0 & g_0 - g_1 g_0^{-1} g_1^\dagger \end{pmatrix} \right] \\ &= \det(g_0) \det(g_0 - g_1 g_0^{-1} g_1^\dagger) \end{aligned} \quad (19)$$

So, we can calculate the edge state spectrum explicitly by solving $\det(g_0 - g_1 g_0^{-1} g_1^\dagger) = 0$. The edge states energy is given by $\varepsilon_\pm(k_1) = \pm \sin(k_1/2)$ with $\varepsilon \in \mathbb{G}$, and $+$ ($-$) corresponds to the state localized at the first (last) layer.

D. Edge state wave vector

We can also calculate the u through Eq. 17. A more convenient method is by extending Bloch's theorem. In our case, we extend the k_2 to the complex domain \mathbb{C} with an analytic continuation, and we have $h_0(k_1, k'_2)u = \varepsilon_+(k_1)u$ with $k_2 \rightarrow k'_2 \in \mathbb{C}$. Then the secular equation gives $\det[\varepsilon_+ - h_0(k_1, k'_2)] = 0$. With k'_2 , u has the form

$$u = \begin{pmatrix} 1 \\ \frac{\varepsilon_+ - d_3(k'_2)}{d_1(k'_2) - i d_2(k'_2)} \end{pmatrix} \quad (20)$$

where the argument k_1 is suppressed. The normalized solution to this equation is $u = \frac{1}{\sqrt{2}} \begin{pmatrix} 1 \\ e^{-i \frac{k_1 - \pi}{2}} \end{pmatrix}^\top$.

Finally, we can use the edge state projector uu^\dagger to construct the effective edge Hamiltonian

$$H_{\text{edge}} = \varepsilon_+ uu^\dagger = \frac{1}{2} \begin{pmatrix} \sin \frac{k_1}{2} & \frac{1}{2}(1 - e^{ik_1}) \\ \frac{1}{2}(1 - e^{-ik_1}) & \sin \frac{k_1}{2} \end{pmatrix}. \quad (21)$$

Another normalized solution with respect to ε_- , i.e., state localized at the last layer, is $u' = \frac{1}{\sqrt{2}} \begin{pmatrix} 1 \\ e^{-i \frac{k_1 + \pi}{2}} \end{pmatrix}^\top$. Taking two edge states together, the effective Hamiltonian is

$$H'_{\text{eff}} = \varepsilon_+ uu^\dagger + \varepsilon_- u' u'^\dagger = \frac{1}{2} \begin{pmatrix} 0 & 1 - e^{ik_1} \\ 1 - e^{-ik_1} & 0 \end{pmatrix} \quad (22)$$

It's very interesting that H'_{eff} is equivalent to the Su-Schrieffer-Heeger model.

III. SELF-ENERGY

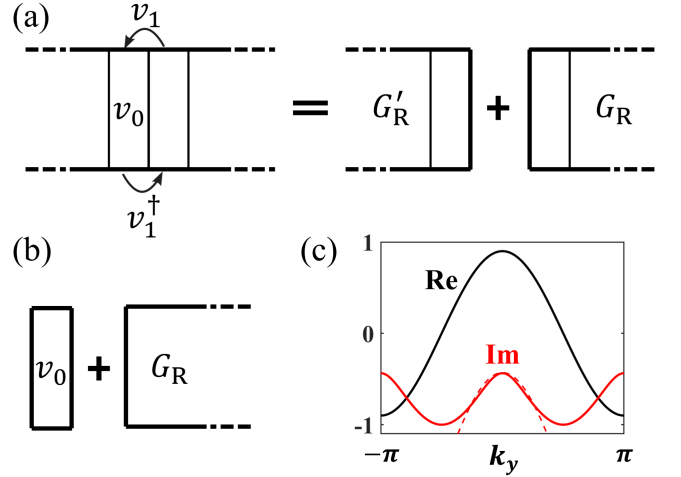


FIG. 3. (a) A full Green's function can be constructed by combining two surface Green's function. (b) The semi-infinite reservoir does not change upon adding another block v_0 . (c) Self-energy of the square lattice (solid lines). $\lambda_1 = 1$, $\lambda_2 = -0.9$ and $\mu = \varepsilon = 0$, hence $\text{Re}(\Sigma) = 0.9 \cos k_y$ and $\text{Im}(\Sigma) \approx 1.13 \cos k_y - 1.56$ around $k_y = 0$ (dashed line).

The formal expression to evaluate the self-energy is $\Sigma = W G_R W^\dagger$, where G_R represents the surface Green's function and W is the coupling between the closed system and the reservoir. A stable algorithm based on the Schur decomposition (as well as the conventional method using the eigendecomposition) to calculate G_R can be found in Ref. [10]. Here, we follow the procedure using the transfer matrix [11].

Constructing blocks from the reservoir lattice, so that the system is periodic in those blocks v_0 and the hopping v_1 between them is restricted to the nearest neighbor, as shown in Fig. 3a. In terms of those blocks, we have the recursion relation of subblock matrix of the Green's function

$$g_{n+1} = v_1^{-1}(\varepsilon - v_0)g_n - v_1^{-1}v_1^\dagger g_{n-1}, \quad (23)$$

which can be rewritten as

$$\begin{pmatrix} g_{n+1} \\ g_n \end{pmatrix} = \begin{pmatrix} v_1^{-1}(\varepsilon - v_0) & -v_1^{-1}v_1^\dagger \\ I & 0 \end{pmatrix} \begin{pmatrix} g_n \\ g_{n-1} \end{pmatrix} \equiv T \begin{pmatrix} g_n \\ g_{n-1} \end{pmatrix}. \quad (24)$$

The above expression requires v_1 is nonsingular. If it is singular, refer to Ref. [8]. Then surface Green's function is obtained from

$$G_R = [\varepsilon - v_0 - v_1 \mathcal{S}_2 \mathcal{S}_1^{-1}]^{-1} \quad (25)$$

or

$$G'_R = [\varepsilon - v_0 - v_1^\dagger \mathcal{S}_3 \mathcal{S}_4^{-1}]^{-1}. \quad (26)$$

G_R or G'_R depends on which semi-infinite part one is interested in (Fig. 3a). $\mathcal{S}_i, i = 1, 2, 3, 4$ is the subblock of the matrix whose column vectors are ordered eigenvectors of T , i.e.,

$$\begin{pmatrix} \mathcal{S}_2 & \mathcal{S}_4 \\ \mathcal{S}_1 & \mathcal{S}_3 \end{pmatrix}^{-1} T \begin{pmatrix} \mathcal{S}_2 & \mathcal{S}_4 \\ \mathcal{S}_1 & \mathcal{S}_3 \end{pmatrix} = \begin{pmatrix} \rho_1 & \\ & \ddots \end{pmatrix}. \quad (27)$$

$(\mathcal{S}_2, \mathcal{S}_1)^T$ corresponds to the eigenvalue $\rho_1 < 1$ and $(\mathcal{S}_4, \mathcal{S}_3)^T$ corresponds to the eigenvalue $\rho_i > 1$ respectively. In general, they are not independent and are related by a symmetry (e.g., inversion symmetry).

The self-energy Σ has a very simple form if one notices the semi-infinite reservoir does not change upon adding another block v_0 . With Σ , the Green's function on the additional block is

$$G_R = (\varepsilon - v_0 + \Sigma)^{-1}. \quad (28)$$

Compare with Eq. 25, we have $\Sigma = -v_1 \mathcal{S}_2 \mathcal{S}_1^{-1}$.

For the lattice Hamiltonian $\mathcal{H}_{\text{Cond}}$ in Eq. 2 in the main text, $v_0 = 2\lambda_2 \cos k_y + \mu$, $v_1 = \lambda_1$, so

$$\Sigma = -\frac{1}{2}(\Lambda + \sqrt{-4\lambda_1^2 + \Lambda^2}) \quad (29)$$

with $\Lambda = \mu - \varepsilon + 2\lambda_2 \cos k_y$.

IV. RESPONSE PROFILE

Here, we give some simple examples to illustrate the response profile, which is an indicator of non-Bloch transport. The model is the Hatano-Nelson model under the

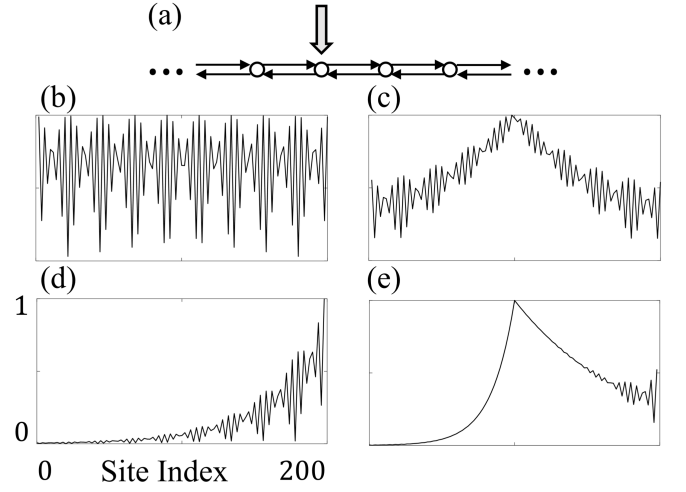


FIG. 4. Response profile corresponding to a unit impulse (Dirac delta function, $E = 0.279$). (a) Hatano-Nelson model. (b) Hermitian case. (c) NH case with global dissipation. (d) Pseudo-Hermitian case. (e) NH case under skin effect and global dissipation.

open boundary condition:

$$\mathcal{H}_{\text{HN}} = \sum_i \left[t e^{i\vartheta} a_i^\dagger a_{i+1} + t e^{-i\vartheta} a_{i+1}^\dagger a_i - i\mu a_i^\dagger a_i \right], \quad (30)$$

where we add the global complex onsite potentials μ . Henceforth we set the nearest neighbor hopping t parameter to unity.

- Hermitian case: $\vartheta = \frac{\pi}{2}$ and $\mu = 0$. The response profile corresponding to an excitation is shown in Fig. 4b, and the excited Bloch wave propagates without attenuation.
- NH case with a global dissipation: $\vartheta = \frac{\pi}{2}$ and $\mu = 0.05$, the eigenvalues of \mathcal{H}_{HN} are in the complex domain owing to μ , but μ does not lead to NH skin effect. As shown in Fig. 4c, the attenuation shows no inclination to the propagation orientation, thus the response profile corresponding to an excitation is $\propto \begin{cases} e^{\beta y}, & y < 0 \\ e^{-\beta y}, & y > 0 \end{cases}, \beta \in \mathbb{R}$, which consists with our intuition of wave attenuation owing to the loss.
- Pseudo-Hermitian case with skin effect: $\vartheta = \frac{\pi}{2} + 0.05i$ and $\mu = 0$, the eigenvalues of \mathcal{H}_{HN} are all real numbers due to pseudo-Hermiticity $\eta^{-1} \mathcal{H}_{\text{HN}} \eta = \mathcal{H}_{\text{HN}}$. The eigenstates pile up at the boundary, exhibiting NH skin effect. The response profile corresponding to a unit excitation is shown in Fig. 4d, and the profile $\propto e^{\alpha y}, \alpha \in \mathbb{R}$ because of the skin effect.
- NH case with both the skin effect and the global dissipation: $\vartheta = \frac{\pi}{2} + 0.05i$ and $\mu = 0.15$. Figure 4e shows the calculated response profile, which

is roughly $\sim \begin{cases} e^{(\alpha+\beta)y}, & y < 0 \\ e^{(\alpha-\beta)y}, & y > 0 \end{cases}$. The decay (or growth) rate is orientation-dependent under the competition between skin effect and global dissipation.

Figure 5 shows some calculated results of the effective chain model (see text around Eq. 5 in the main text).

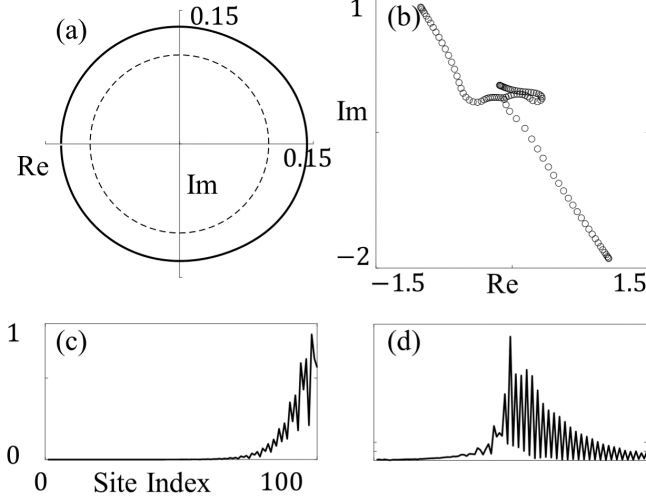


FIG. 5. Calculated results of the effective chain model. (a) Generalized Brillouin zone. In plotting, we use $(|\beta| - 0.99)e^{i\text{Arg}(\beta)}$, $\beta = e^{i\tilde{k}}$ in which \tilde{k} is the complex wave number. (b) Eignvalues of the chain Hamiltonian with open boundaries. (c) Eigenvector with respect to the eigenvalue $E = 0$. (d) Response profile corresponding to a unit impulse ($E = 0.028$)

V. REALIZATION OF THE HOPPING WITH A PHASE

Our previous works [12, 13] develop a correspondence between circuit networks and tight-binding lattice models. We want to apply this theory to higher-frequency regions, such as radio and optical frequencies. Higher frequencies imply decreasing wavelengths. This follows that voltages and currents no longer remain spatially uniform when compared to the geometric size of the discrete circuit elements. As a consequence, they have to be treated as propagating waves. Since Kirchhoff's voltage and current laws do not account for these spatial variations, we must significantly adjust the analysis from conventional lumped to distributed circuit representation.

Multiple port networks are essential tools in restructuring and simplifying complicated circuits as well as in providing key insight into the performance of devices. To describe such network input-output parameter relations, we have impedance, admittance, S-parameter, hybrid, and ABCD parameters—conversions exist between these sets. However, some relations may not be well-defined,

such as the admittance of a circulator (see subsection 1), causing difficulty in finding the correspondence between higher-frequency networks and tight-binding lattice models. The principal advances of the S-parameter are that: (i) it is always well-defined in a passive device; (ii) the experimental determination of it is convenient without the need to know the internal structure of the device. Here, we show how to realize the hopping with a phase (we set the coupling amplitude to unity) in the TTC network by designing the S-parameter (see subsection 2-4) when the admittance of the device is not available. The phased-hopping breaks the reciprocity, i.e., $t_{ij} \neq t_{ji}$, so we use a circulator to realize this hopping. The ‘black box’ treatment of the S-parameter indicates that distinct devices or different network configurations can realize the same phased-hopping since they may have an identical S-parameter (see subsection 4). The calculation of S-parameters is based on the signal flow graph, subsection 2 will provide some context.

A. Ill-defined admittance of microwave circulators

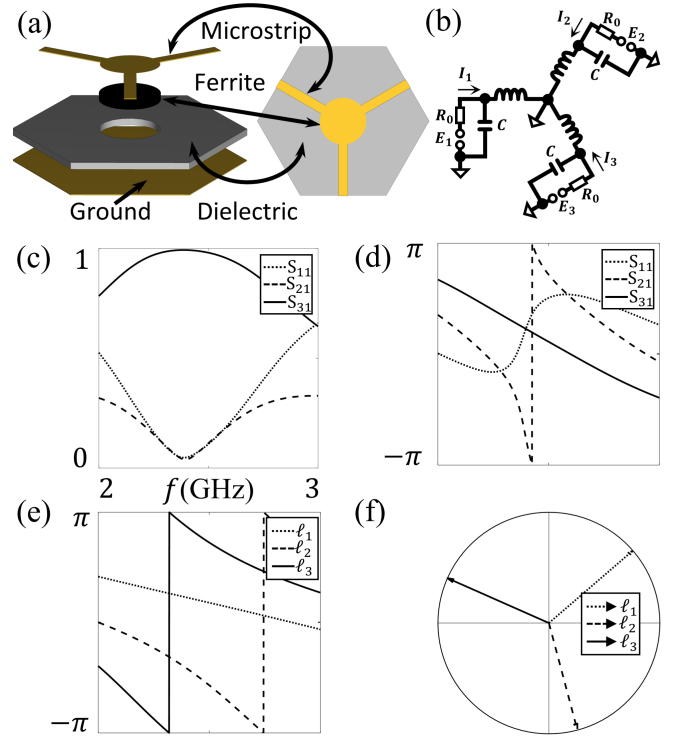


FIG. 6. (a) Schematic of a three-port microstrip circulator. (b) Shunt network of lumped element circulator. (c) and (d) Scattering parameters (amplitude and phase) of the circulator from CST simulation. (e) Characteristics (ℓ_1, ℓ_2, ℓ_3) as function as the frequency varies, the circulator resonates at 2.4 GHz. (f) Eigenvalues of the scattering matrix at 2.4 GHz, $u^{-1}Su = \text{diag}(e^{i\ell_1}, e^{i\ell_2}, e^{i\ell_3})$, where $(\ell_1, \ell_2, \ell_3) = (\ell_0, \ell_0 + \frac{2\pi}{3}, \ell_0 - \frac{2\pi}{3})$ and $\ell_0 \approx 0.71$.

The circulator geometry (Fig. 6a) can readily be analyzed using the lumped element configuration (Fig. 6b illustrates the network). The usual arrangement consists of a ferrite disk with three strips wound on it: i) the strips are oriented at 120° with respect to each other and are electrically short at the end of them; ii) a direct magnetic field H_0 is applied normal to the plane of the circulator, so the relative permeability tensor μ_{ij} of the ferrite disk is

$$[\mu_{ij}] = \begin{pmatrix} \mu & -i\kappa & 0 \\ i\kappa & \mu & 0 \\ 0 & 0 & 1 \end{pmatrix}. \quad (31)$$

with

$$\begin{aligned} \mu &= 1 + \frac{\omega_0 \omega_m}{\omega_0^2 - \omega^2}, \\ \kappa &= \frac{\omega \omega_m}{\omega^2 - \omega_0^2}. \end{aligned} \quad (32)$$

$\omega_0 = \gamma(H_0 - N_z M_s)$, and $\omega_m = \gamma M_s$, where M_s is the saturation magnetization, γ is the gyromagnetic ratio, N_z is the demagnetizing factor. The presence of imaginary off-diagonal components having opposite signs in μ_{ij} is the basis for the nonreciprocal effect.

The energy within the disk is essentially magnetic because of shorted strips. That follows that the simplified equivalent circuit in the disk, which retains all of the electrical characteristics, contains three mutual inductances. Shunt capacities out of the disk are added to maintain the characteristic impedance. So, the voltage-current relationships (impedance) at the terminals of the disk structure are

$$\begin{pmatrix} V_1 \\ V_2 \\ V_3 \end{pmatrix} = i\omega L_0 \begin{pmatrix} \mu & \frac{i\kappa - \mu}{2} & \frac{-i\kappa - \mu}{2} \\ \frac{-i\kappa - \mu}{2} & \mu & \frac{i\kappa - \mu}{2} \\ \frac{i\kappa - \mu}{2} & \frac{-i\kappa - \mu}{2} & \mu \end{pmatrix} \begin{pmatrix} I_1 \\ I_2 \\ I_3 \end{pmatrix} \equiv Z \begin{pmatrix} I_1 \\ I_2 \\ I_3 \end{pmatrix}. \quad (33)$$

Note that $Z \neq Z^T$ as $\mu_{ij} \neq \mu_{ji}$.

The admittance of the circulator, which is the inverse of Z , is ill-defined since its impedance Z is singular (i.e., the voltages do not determine the currents). Nevertheless, we can calculate the pseudoinverse of Z ,

$$Z^+ = \frac{4\mu}{3(-\kappa^2 + 3\mu^2)} \frac{1}{i\omega L_0} \begin{pmatrix} \mu & \frac{-i\kappa - \mu}{2} & \frac{i\kappa - \mu}{2} \\ \frac{i\kappa - \mu}{2} & \mu & \frac{-i\kappa - \mu}{2} \\ \frac{-i\kappa - \mu}{2} & \frac{i\kappa - \mu}{2} & \mu \end{pmatrix}. \quad (34)$$

One can hardly find any correspondence to \mathcal{H}_Δ .

The scattering matrix S however is well-defined (note that every passive circuit has a scattering matrix [14]), and $SS^\dagger = 1$ if the network is dissipationless. The circulator respects C3 symmetry, thus we can use the frame u defined in the main text to diagonalize the matrix, $u^{-1}Su = \text{diag}(e^{i\ell_1}, e^{i\ell_2}, e^{i\ell_3})$. This also follows that $S_{11} = S_{22} = S_{33}$, $S_{12} = S_{23} = S_{31}$ and $S_{21} = S_{32} = S_{13}$. Similarly, the eigenvalues uniquely define the scattering relation between ports.

Figure 6c and d show the scattering parameters of the circulator and its characteristics as frequency varies. At the resonant frequency of the circulator, the scattering matrix is approximate to an ideal circulator:

$$S_{\text{id}} = e^{i\ell_0} \begin{pmatrix} 0 & 0 & 1 \\ 1 & 0 & 0 \\ 0 & 1 & 0 \end{pmatrix}, \quad (35)$$

and the characteristics are $(\ell_1, \ell_2, \ell_3) = (\ell_0, \ell_0 + \frac{2\pi}{3}, \ell_0 - \frac{2\pi}{3})$.

B. Review of signal flow graphs

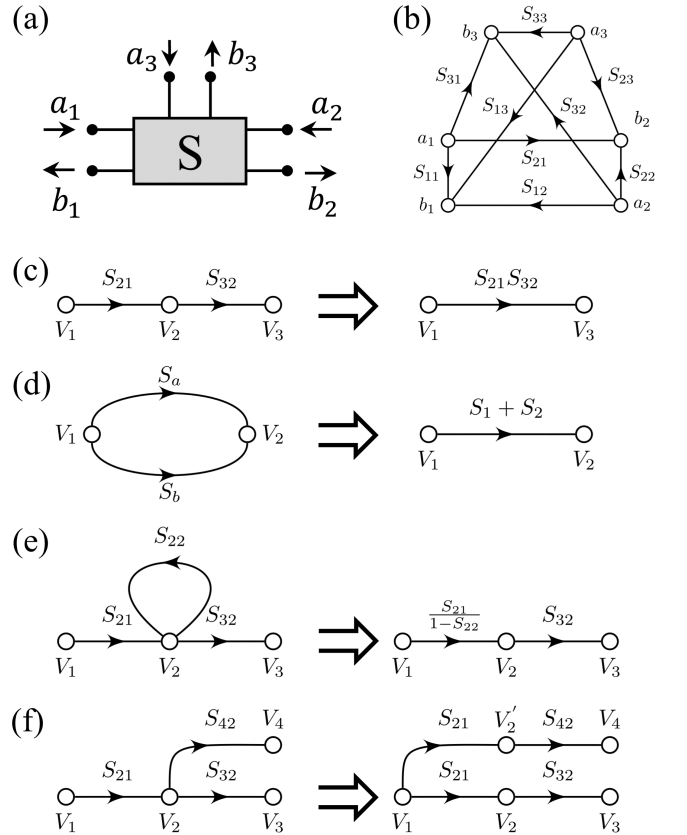


FIG. 7. The signal flow graph representation of a three-port network and decomposition rules of flow graph. (a) A general three-port network and (b) its signal flow graph. Decomposition rules: (c) Series rule, (d) Parallel rule, (e) Self-loop rule, (f) Splitting rule.

The analysis of networks is greatly facilitated through signal flow graphs. The primary components of the graph are nodes and branches. Each port i of a network has two nodes: node a_i is deployed to identify an entering wave, while b_i is a reflected wave. A branch is a directed path between two nodes representing signal flow from one node to another. The S-parameter (the scattering

matrix, e.g., Fig. 7a and b) is defined as

$$\begin{aligned} S_{ii} &= \frac{b_i}{a_i} \bigg|_{a_{j \neq i}=0}, \\ S_{ji} &= \frac{b_j}{a_i} \bigg|_{a_{l \neq i}=0}. \end{aligned} \quad (36)$$

In the network, we use the normalized incident power wave a_i and reflected power wave b_i :

$$\begin{aligned} a_i &= \frac{1}{2\sqrt{Z_0}}(V_n + Z_0 I_n), \\ b_i &= \frac{1}{2\sqrt{Z_0}}(V_n - Z_0 I_n), \end{aligned} \quad (37)$$

where the Z_0 is the characteristic impedance of the connecting waveguide on the input and output side of the network. In what follows, we set $Z_0 = 1$ for simplicity. A signal flow graph can be reduced to a single branch between two nodes using the four basic decomposition rules to obtain any desired wave amplitude ratio (Fig. 7c-f).

C. Two sites

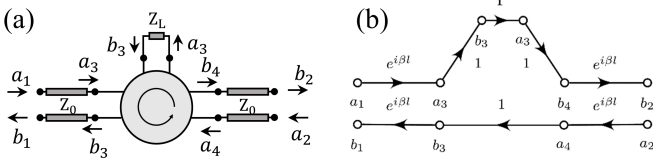


FIG. 8. Realization of two-site hopping with a phase. (a) Schematic of the realization. (b) Corresponding flow graph.

We employ a three-port ideal circulator (we set $\ell_0 = 0$ in Eq. 35) to realize the two-site coupling with an arbitrary phase θ and set the coupling amplitude to unity. The Hamiltonian of the two sites reads

$$\mathcal{H}_2 = \begin{pmatrix} & e^{i\theta} \\ e^{-i\theta} & \end{pmatrix}. \quad (38)$$

The bilinear transform $\frac{i+\mathcal{H}_2}{i-\mathcal{H}_2}$ gives $\begin{pmatrix} & e^{i(\theta-\frac{\pi}{2})} \\ e^{i(\frac{\pi}{2}-\theta)} & \end{pmatrix}$.

One can not find a θ -independent frame that diagonalizes the transformed matrix, but we can define two characteristics χ_{\pm} as $\chi_{\pm} = \pm(\theta - \frac{\pi}{2})$ by noting the off-diagonal form of the transformed matrix.

Two ports of the circulator are attached to the waveguides with electrical length βl , where β is the wavenumber in the waveguide and l is the physical length of the waveguide, and the rest port is terminated in a load impedance Z_L . Using the flow graph Fig. 8b, the S-parameter of this configuration is

$$S_2 = \begin{pmatrix} & e^{2i\beta l} \\ \Gamma e^{2i\beta l} & \end{pmatrix}, \quad (39)$$

where $\Gamma = \frac{Z_L - Z_0}{Z_L + Z_0}$ is the reflection coefficient. Unitary matrix $S_2 S_2^\dagger = 1$ leads to $|\Gamma| = 1$. Similarly, we can define the characteristics of S_2 as $\ell_+ = 2\beta l$ and $\ell_- = \text{Arg}(\Gamma) + 2\beta l$. χ_{\pm} and ℓ_{\pm} give us the correspondence, for example, when $\theta = \frac{\pi}{2}$, $\beta l = 0$, $Z_L = 0$. Note that the load Z_L can be realized by a piece of waveguide with its end grounded or open (see Fig. 12 and text around there).

D. Three sites

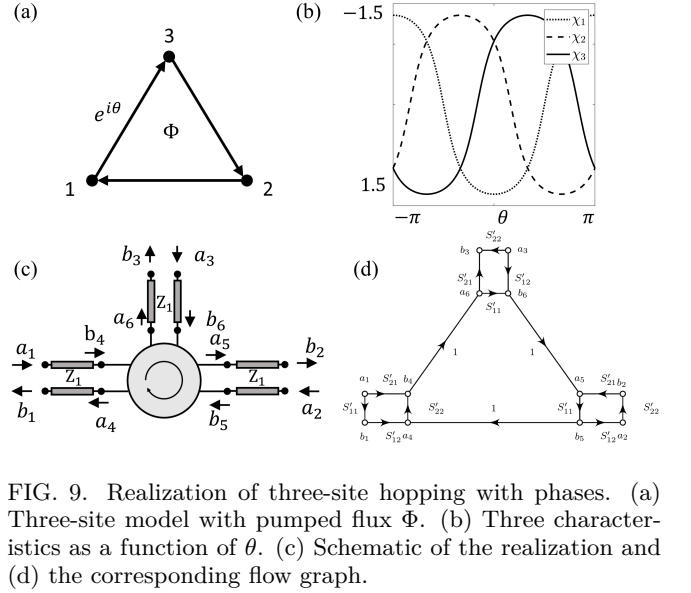


FIG. 9. Realization of three-site hopping with phases. (a) Three-site model with pumped flux Φ . (b) Three characteristics as a function of θ . (c) Schematic of the realization and (d) the corresponding flow graph.

Here, we show how to realize the next-nearest neighbor hopping required in the Haldane model. To illustrate it, consider the following three-site Hamiltonian (Fig. 9a):

$$\mathcal{H}_\Delta = \begin{pmatrix} 0 & e^{i\theta} & e^{-i\theta} \\ e^{-i\theta} & 0 & e^{i\theta} \\ e^{i\theta} & e^{-i\theta} & 0 \end{pmatrix}. \quad (40)$$

The transformed matrix $\mathcal{S} = \frac{i+\mathcal{H}_\Delta}{i-\mathcal{H}_\Delta}$ can be diagonalized by the frame u because of the C3h symmetry: $u^{-1}\mathcal{S}u = \text{diag}(e^{i\chi_1}, e^{i\chi_2}, e^{i\chi_3})$, where $u = (\mathbf{v}_1, \mathbf{v}_2, \mathbf{v}_3)$, $\mathbf{v}_1 = (1, 1, 1)^T$, $\mathbf{v}_2 = (1, \alpha, \alpha^2)^T$, $\mathbf{v}_3 = (1, \alpha^2, \alpha)^T$ with $\alpha = e^{\frac{2\pi i}{3}}$. The characteristics are shown in Fig. 9b as θ varies.

To realize that, we employ a three-port circulator with its ports attached to waveguides, see Fig. 9c. The waveguides attached have the characteristic impedance of Z_1 , and the electrical length is $\beta_1 l_1$. Using the flow graph

Fig. 9d, the S-parameter of this configuration is

$$\begin{aligned} S_{11} &= \frac{a(a^3 - ab^2 - 1)}{a^3 - 1} \\ S_{12} &= \frac{-ab^2}{a^3 - 1} \\ S_{21} &= \frac{-b^2}{a^3 - 1}, \end{aligned} \quad (41)$$

and $S_{11} = S_{22} = S_{33}$, $S_{12} = S_{23} = S_{31}$ and $S_{21} = S_{32} = S_{13}$ due to C3 symmetry of the configuration (i.e. S is a circular matrix denoted as $S = \text{circ}(S_{11}, S_{12}, S_{13})$). $S' = \begin{pmatrix} a & b \\ b & a \end{pmatrix}$ is the scattering matrix because of the impedance mismatch between connecting waveguides of Z_0 and attached waveguides of Z_1 , $a = e^{i\beta_1 l_1} \frac{Z_0 - Z_1}{Z_0 + Z_1}$. The mirror symmetry of the impedance-mismatch scattering leads to $S'_{12} = S'_{21}$ and $a^2 + b^2 = 1$ follows from $S' S'^\dagger = 1$. The characteristics of S-parameter $\ell_{1,2,3}$ (i.e., the eigenvalues of the S-parameter) and characteristics of transformed-matrix $\chi_{1,2,3}$ give the correspondence, for example, when $\theta = \frac{\pi}{2}$, $\beta_1 l_1 = 0$, $Z_1 = Z_0$.

What is unique to the three-port ideal circulator is that we can calculate its admittance through $Y_{\text{id}} = \frac{1 - S_{\text{id}}}{1 + S_{\text{id}}}$ (set $\ell_0 = 0$). An alternative approach to calculating this diagram structure (Fig. 9a) using the Kirchhoff's law can be found around Eq. 58.

E. Four sites

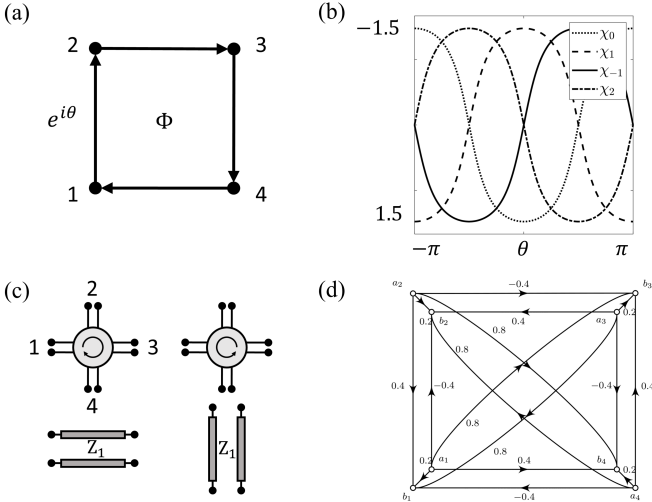


FIG. 10. Realization of four-site hopping with phases. (a) Four-site model with pumped flux Φ . (b) Four characteristics as a function of θ . (c) Schematic of the realization by the channel decomposition and (d) the corresponding flow graph.

Here, we show how to introduce the flux through a four-site plaquette. Without losing generality, we set the coupling amplitude to be unity and the onsite potential

to be zero (Fig. 10a). The resulting Hamiltonian is

$$\mathcal{H}_{\square} = \begin{pmatrix} 0 & e^{i\theta} & 0 & e^{-i\theta} \\ e^{-i\theta} & 0 & e^{i\theta} & 0 \\ 0 & e^{-i\theta} & 0 & e^{i\theta} \\ e^{i\theta} & 0 & e^{-i\theta} & 0 \end{pmatrix}. \quad (42)$$

When $\Phi = 0$, the model respects D4h symmetry, So according to group theory, we can generate the equivalence representation (i.e., transform between equivalent sites) for the symmetry. In this case, the equivalence representation Γ is reducible:

$$\Gamma = A_1 \oplus B_1 \oplus E \quad (43)$$

where A_1 , B_1 and E denote the irreducible representation of D4h. E is a 2-by-2 matrix, meaning that two of the four eigenvalues of \mathcal{H}_{\square} are degenerate. Those two-fold eigenvalues can be lifted by pumping flux Φ , and \mathcal{H}_{\square} respects C4 symmetry when pumping. So we can use a symmetrical set of basis

$$u = \begin{pmatrix} 1 & 1 & 1 & 1 \\ 1 & -1 & i & -i \\ 1 & 1 & -1 & -1 \\ 1 & -1 & -i & i \end{pmatrix}. \quad (44)$$

Under this frame u , the transformed matrix $\mathcal{S} = \frac{i + \mathcal{H}_{\square}}{i - \mathcal{H}_{\square}}$ can be diagonalized as $u^{-1} \mathcal{S} u = \text{diag}(e^{i\chi_0}, e^{i\chi_1}, e^{i\chi_{-1}}, e^{i\chi_2})$. Those characteristics are shown in Fig. 10b as θ varies.

One of the simplest ways to realize \mathcal{H}_{\square} is by taking advantage of two-site coupling (see text around Eq. 38). Here, we introduce the other two ways. Without losing generality, we set $\theta = \frac{\pi}{2}$ in the following.

I—If the S-parameter shares the same characteristics as \mathcal{S} , S will take the form $S = u \cdot \text{diag}(e^{i\chi_0}, e^{i\chi_1}, e^{i\chi_{-1}}, e^{i\chi_2}) \cdot u^{-1}$. $S = \text{circ}(0.2, -0.4, 0.8, 0.4)$ when $\theta = \frac{\pi}{2}$. We can decompose S into several channels, $S = S_{\circlearrowleft} + S_{\circlearrowright} + S_{\nearrow} + S_{\searrow}$ where $S_{\circlearrowleft} = -0.4 \cdot \text{circ}(0, 1, 0, 0)$, $S_{\circlearrowright} = 0.4 \cdot \text{circ}(0, 0, 0, 1)$,

$$S_{\nearrow} = \begin{pmatrix} 0.2 & 0.8 \\ 0.8 & 0.2 \end{pmatrix} \text{ and } S_{\searrow} = \begin{pmatrix} 0.2 & 0.8 \\ 0.8 & 0.2 \end{pmatrix}. \quad (45)$$

By inspection, we find that S_{\circlearrowleft} and S_{\circlearrowright} are nothing but the S-parameters of four-port right-hand and left-hand circulators. S_{\nearrow} or S_{\searrow} corresponds to the reciprocal scattering between port-1 and port-3 or scattering between port-2 and port-4 (Fig. 10c). This construction can be easily verified by the signal flow graph shown in Fig. 10d.

II—The above realization is still cumbersome for experiments. The construction discussed here is based on the ferrite eigenvalue adjustment for the 4-port nonreciprocal devices [15–17]. The geometry of a dielectric disk is shown in Fig. 11a. Here, we focus on the resonant modes $\text{HE}_{\pm 1,1,1}$ supported by the disk. Without the external magnetic field, two modes are degenerate due to

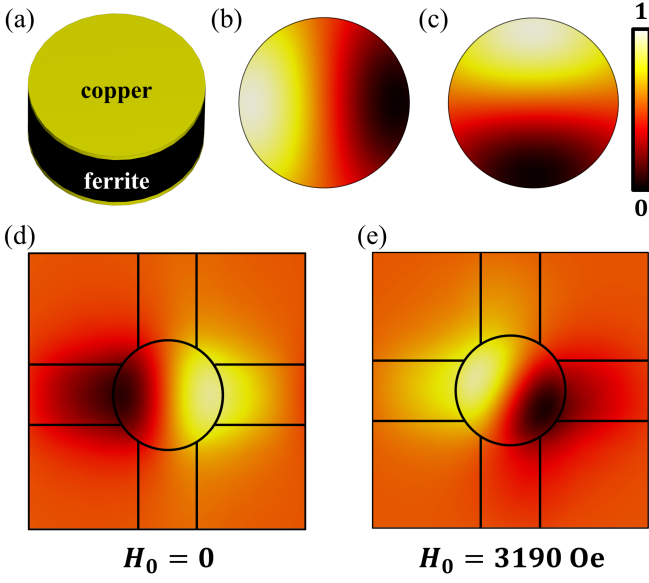


FIG. 11. Realization of Four-site hopping by the ferrite eigenvalue adjustment. (a) Geometry of a dielectric disk. (b) and (c) Field patterns of $HE_{\pm 1,1,1}$. (d) Scattering field distribution without external magnetic field. (e) Scattering field distribution under external magnetic field. Parameters of the ferrite are $\epsilon_f = 25$, $4\pi M_s = 1800$ Gauss, $\Delta H = 18$ Oe, and the radius of the disk is 2 mm.

the cylinder symmetry of the disk, and their field patterns resemble the p_x and p_y orbitals of an atom (Fig. 11b and c). If we attach four ports to this disk under the C_4 symmetry, the S-parameter between ports around the $HE_{\pm 1,1,1}$ eigenfrequency is $S = \text{circ}(0, 0, 1, 0)$. This follows that the excitation from one port only excites one mode of $HE_{\pm 1,1,1}$. For example, excitation from port 1 can only excite $HE_{1,1,1}$ mode, so it only couples to port 3, and there is no cross-over between channel $1 \leftrightarrow 3$ and channel $2 \leftrightarrow 4$ (Fig. 11d).

Correspondingly, the characteristics of $\text{circ}(0, 0, 1, 0)$ are $(\ell_0, \ell_1, \ell_{-1}, \ell_2) = (0, \pi, \pi, 0)$, $\ell_+ = \ell_-$ because of the D_{4h} symmetry, $\ell_1 = \ell_2$ because of the accidental degeneracy. Those characteristics can be adjusted by the amplitude of the direct magnetic field. This adjustment rotates the standing wave formed by $HE_{1,1,1}$ to make sure $\ell_{\pm 1} = \pm 0.7048\pi$ (Fig. 11e), and it lifts the degeneracy of ℓ_1 and ℓ_{-1} without affecting ℓ_0 and ℓ_2 .

VI. SIMULATIONS OF MICROSTRIP LINE METAMATERIALS

This section gives the details about simulations of the metamaterials. Firstly, we use microstrip line (ML) to demonstrate the flexibility of TTCs to upgrade to higher frequencies. The ML circuit also exhibits the property of momentum resolution, which is the advantage of TTCs and is demonstrated through ML honeycomb lattice model. Then, the admittance properties of a circuit

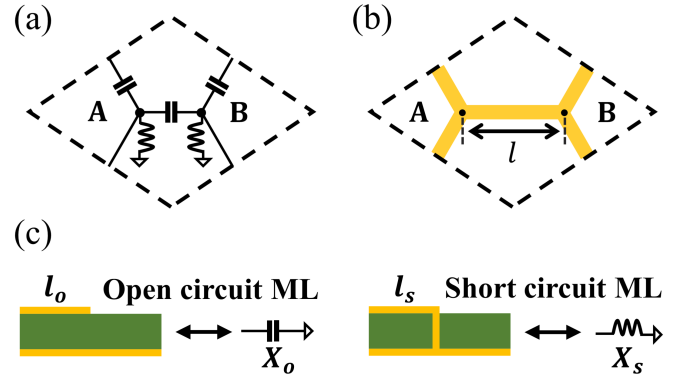


FIG. 12. (a) Unit cell of the circuit honeycomb lattice. (b) Unit cell of ML honeycomb lattice. (c) The equivalent circuit of a red triangle part in (b). (d) The equivalent circuits of open and short circuit ML.

lattice are analyzed in order to construct Haldane model with ML. Moreover, details about the microwave field-circuit co-simulation of the ML junction are given.

A. Upgrade of TTCs

To construct the topological junction, we first consider the honeycomb lattice with only the nearest neighbor hopping t_1 and onsite potential μ , which is the basis of Haldane model. The Hamiltonian of such lattice reads

$$\mathcal{H}_{\text{Gra}} = t_1 \sum_{\langle i,j \rangle} c_i^\dagger c_j + \mu \sum_i c_i^\dagger c_i \quad (46)$$

and can be realized with temporal topoelectrical circuits (TTCs). The unit cell of the corresponding circuit lattice is shown in Fig. 12a. The distance between the sublattices A and B is set to be 1. Thus, the lattice constant is $\sqrt{3}$ and the admittance matrix J_{Gra} in momentum space reads

$$J_{\text{Gra}} = -i\omega C_1 \begin{pmatrix} 0 & J_{12} \\ J_{12}^\dagger & 0 \end{pmatrix} + (3i\omega C_1 + \frac{1}{i\omega L_1}) \mathbb{I}_2$$

$$J_{12} = 1 + e^{\frac{i}{2}(\sqrt{3}k_x + 3k_y)} + e^{\frac{i}{2}(-\sqrt{3}k_x + 3k_y)}, \quad (47)$$

where ω is the operating angular frequency and \mathbb{I}_n is the n -by- n identity matrix. Generally, the nearest neighbor hopping t_1 is realized with the capacitor C_1 and the onsite potential is adjusted through the grounded inductor L_1 .

As stated in the main text, TTCs can be upgraded to the microwave domain. Such upgrade is practical for many platforms, e.g., waveguide, coaxial line, ML and so on, and we use ML to illustrate the procedure. ML consists of a dielectric substrate with a conductor strip attached to its surface and the ground plane on the other. Under a certain parameter range, the electromagnetic properties of an ML with width w and length l are equivalent to a Π -shaped circuit as shown in Fig. 4a and 4b in

the main text. The admittances of the components are

$$\begin{aligned} X_1 &= -i \frac{1}{Z_0 \sin k_0 l}, \\ X_2 &= i \frac{1}{Z_0} \tan \frac{k_0 l}{2}, \end{aligned} \quad (48)$$

where Z_0 is the characteristic impedance and $k_0 = 2\pi/\lambda_0$ is the wave number. The ML parameters are $w = 2.2$ mm, $l = 16.3$ mm, $h = 1.2$ mm, $\varepsilon_r = 4.6$, and $f = 2.4$ GHz, which lead to the impedance $Z_0 = 50 \Omega$ and the electrical length $k_0 l = \pi/2$. Thus, $X_1 + X_2 = 0$, the self-admittance of both sublattice A and B is equal to 0.

Because of the equivalence, the circuit cell of Fig. 12a can be replaced by ML as shown in Fig. 12b. We construct the ML honeycomb lattice in CST (Fig. 13a) and simulate the field distribution. A waveguide port is set at P and the field within the green box is simulated at $f = 2.4$ GHz. All boundaries are set as perfect electric conductors.

After Fourier Transform (FT), the energy band section at certain momentum is achieved (Fig. 13b). The theoretical result calculated from Eq. 46 is also given for comparison. As an upgrade of TTCs, the ML lattice also exhibits the property of momentum resolution. The momentum at which the band section is obtained after FT can be adjusted by attaching a length of open or short circuit ML to sublattice sites. As shown in Fig. 12c, a length of open (short) circuit ML is equivalent to a grounded capacitor (inductor), whose admittance is

$$\begin{aligned} X_o &= i \frac{1}{Z_0} \tan k_0 l_o, \\ X_s &= -i \frac{1}{Z_0 \tan k_0 l_s}. \end{aligned} \quad (49)$$

Therefore, attaching a length of ML to a site simply alters the self-admittance of it, changing the onsite potential μ . To demonstrate that, simulation at different onsite potentials is caused (Fig. 13c and 13d).

B. ML Haldane model

To make honeycomb lattice topological, imaginary next-nearest neighbor hopping related with direction is added to break the time-reversal symmetry, which is the Haldane model. For ML lattice, such hopping can be introduced through a circulator (Fig. 14a). The propagation of wave in a circulator depends on the location of the three ports. For an ideal circulator, the S matrix is

$$S_{\text{cir}} = \begin{pmatrix} 0 & 0 & 1 \\ 1 & 0 & 0 \\ 0 & 1 & 0 \end{pmatrix} \quad (50)$$

and the corresponding admittance matrix is

$$J_{\text{cir}} = \frac{1}{Z_0} \begin{pmatrix} 0 & 1 & -1 \\ -1 & 0 & 1 \\ 1 & -1 & 0 \end{pmatrix} = i \frac{1}{Z_0} \begin{pmatrix} 0 & -i & i \\ i & 0 & -i \\ -i & i & 0 \end{pmatrix}. \quad (51)$$

However, an actual circulator always carries a phase shift of θ and the corresponding S and admittance matrices are

$$S_{\text{act}} = \begin{pmatrix} 0 & 0 & e^{i\theta} \\ e^{i\theta} & 0 & 0 \\ 0 & e^{i\theta} & 0 \end{pmatrix}, J_{\text{act}} = \frac{\mathbb{I}_3 - S_{\text{act}}}{Z_0(\mathbb{I}_3 + S_{\text{act}})}. \quad (52)$$

Moreover, connecting circulators to the lattice sites also requires certain lengths of ML. To calculate the overall admittance J'_{cir} introduced by an actual circulator, the schematic is shown as Fig. 14b. I and V are the current and voltage respectively, and l' is the length of the connecting ML. The corresponding admittance X'_1 and X'_2 can be calculated as Eq. 48. Denoting $I = [I_1 \ I_2 \ I_3]^T$ and the same for V , I' , and V' , then

$$I' = X'_1 V' + X'_2 (V' - V), \quad (53)$$

$$X'_2 (V' - V) = X'_1 V + I. \quad (54)$$

Noting that $I = J_{\text{act}} V$,

$$I' = X'_1 V' + X'_1 V + J'_{\text{cir}} V, \quad (55)$$

and Eq. 54 can be transformed into

$$V = \left(\frac{X'_1 \mathbb{I}_3 + J_{\text{act}}}{X'_2} + \mathbb{I}_3 \right)^{-1} V'. \quad (56)$$

Substituting Eq. 56 into Eq. 55,

$$I' = \left(X'_1 + \frac{X'_1 \mathbb{I}_3 + J_{\text{act}}}{\frac{X'_1 \mathbb{I}_3 + J_{\text{act}}}{X'_2} + \mathbb{I}_3} \right) V', \quad (57)$$

namely

$$J'_{\text{cir}} = X'_1 + \frac{X'_1 \mathbb{I}_3 + J_{\text{act}}}{\frac{X'_1 \mathbb{I}_3 + J_{\text{act}}}{X'_2} + \mathbb{I}_3}. \quad (58)$$

Introducing the imaginary next-nearest neighbor hopping to the ML honeycomb lattice with circulators, the ML Haldane lattice with armchair boundaries is constructed as shown in Fig. 15a. The ML Haldane lattice consists of 2 layers (only shown in the inset without substrates and ground plane for clarity): three non-adjacent sites are connected to a ferrite circulator on the top layer, and the other three are connected to another circulator on the bottom layer through vias. The two layers are separated by copper, which serves as the ground plane. Figure 15b shows the corresponding field distribution at $f = 2.4$ GHz, which demonstrates the existence of boundary state. It should be noted that, in simulations, we use ML ferrite circulators as Fig. 6a, while for experimental realization, commercial circulators as Fig. 14a can be used directly to simplify the structure.

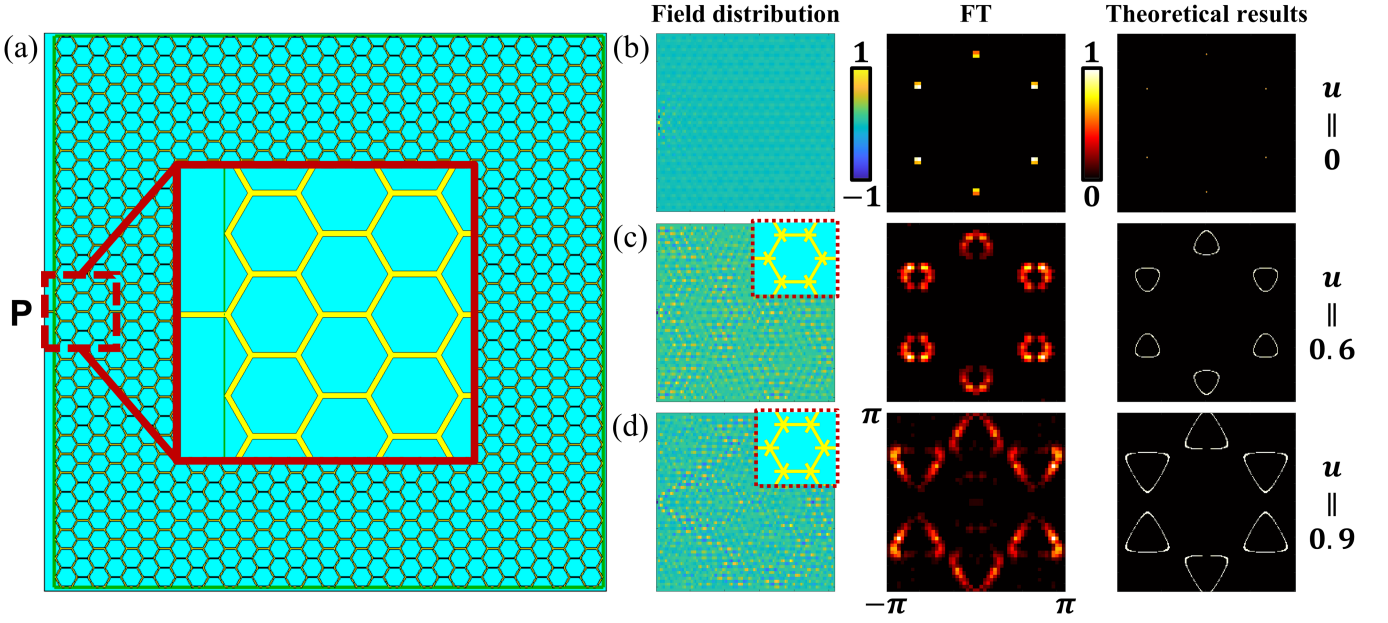


FIG. 13. (a) Simulation model of ML honeycomb lattice. (b)-(d) Simulated field distributions and the corresponding energy band sections at different onsite potentials. Theoretical results are given for comparison.

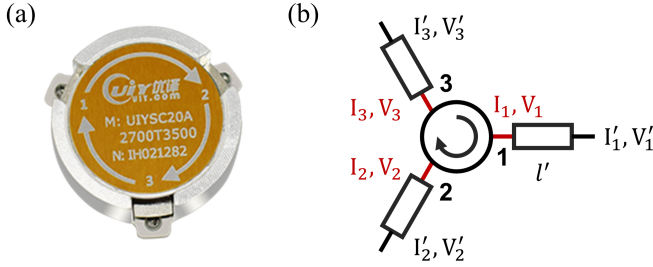


FIG. 14. (a) A circulator. (b) Schematic of connecting a circulator to ML lattice with three lengths of ML.

C. Field-circuit co-simulation of the junction

Connecting conductors at the boundary of the ML Haldane model can construct the junction. However, due to the large scale and complex multi-layer and thin-layer structures of the junction, simulating a complete model requires extremely high-density meshing and massive computational resources. In addition, we only care about the propagation characteristics of electromagnetic wave within the junction regions rather than the field distributions of the entire model. Thus, we adopt the CST microwave field-circuit co-simulation method to simplify computation and solve the transmission behavior.

Specifically, the model is roughly divided into four parts as shown in Fig. 16:

The component shown in Fig. 16a contains two sub-lattice sites A and B of the honeycomb lattice. The area indicated by red solid lines (namely, port 1, 3, 6, 8) represents the connection between adjacent sites,

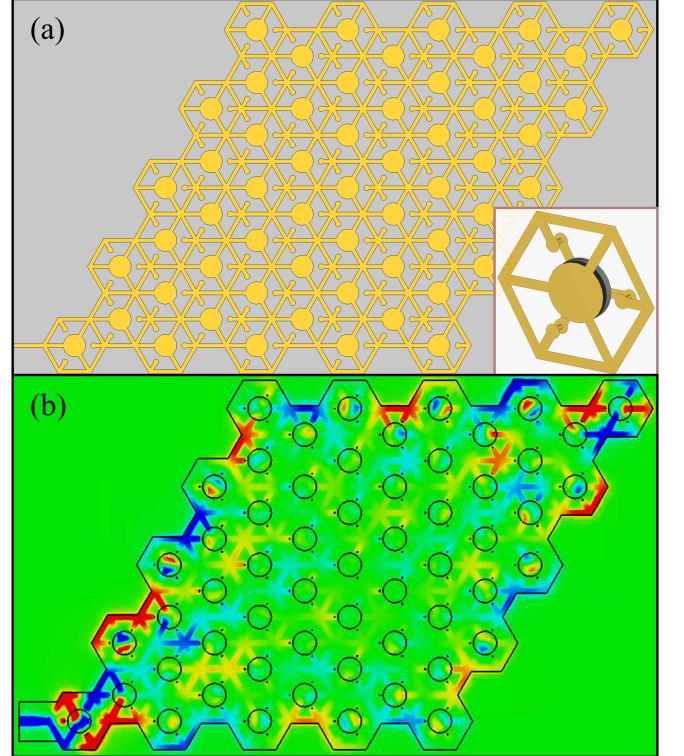


FIG. 15. (a) The simulation model of ML Haldane lattice. (b) Field distribution at $f = 2.4$ GHz.

while the other ports are used to connect the sites with circulators. Key simulation parameters are ML width $w = 2.2$ mm, distance between adjacent sites $l_{AB} =$

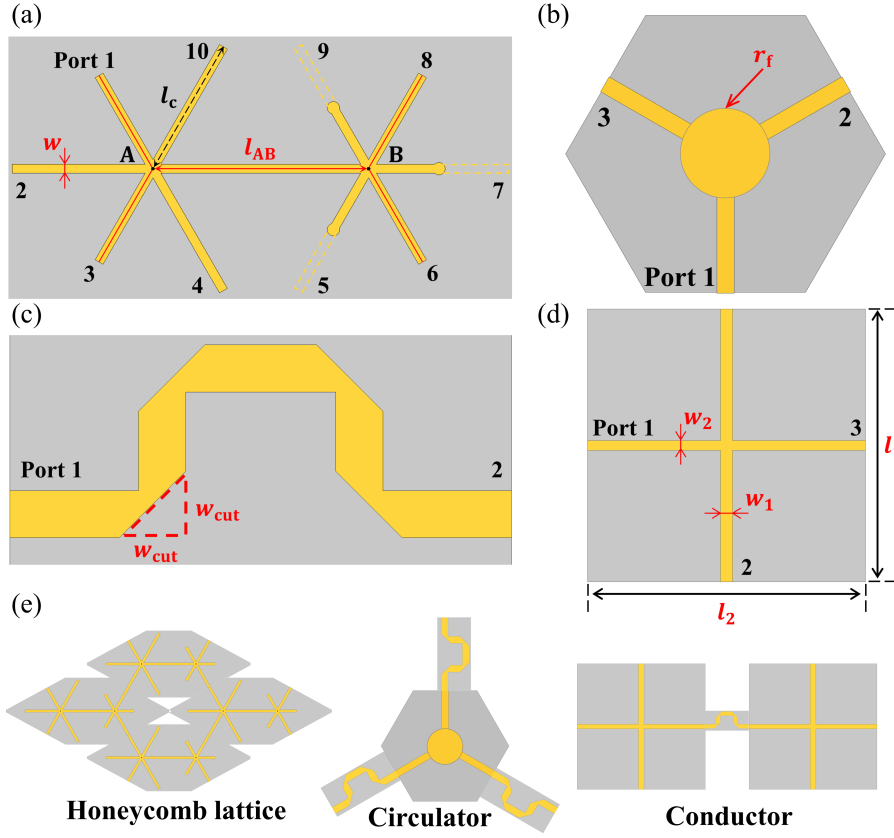


FIG. 16. Schematic of the field-circuit co-simulation. (a) Blocks used to construct honeycomb lattice and connect lattice sites with circulators. (b) Circulators. (c) Blocks used to adjust the electrical length between two sites at a fixed distance. (d) Blocks used for conductors. (e) Examples of assembling the blocks. All the blocks have undergone microwave electromagnetic simulation to solve the S-parameters among corresponding ports. Then they are assembled into the junction.

52.2 mm. The length of the lines connected to circulators is $l_c = 34.1$ mm. It should be noted that, such lines (namely, port 2, 4, 5, 7, 9, 10) are set only for the calculation of S-parameters, which are necessary in the co-simulation. However, when constructing the complete model or in experiment, they can be removed and connect sublattice sites with circulators directly.

Figure 16b is a circulator with the same line width of w . Parameters of the ferrite is radius $r_f = 5$ mm, dielectric constant $\epsilon_f = 37.4$, Saturation magnetization $4\pi M_s = 1800$ Gauss and the external magnetic field $H_z = -2120$ Oe.

Figure 16c shows the right-angle bending design of ML, which is used to achieve variable electrical length between two sites with a fixed spatial distance. The key parameter of this structure is the cutting width $w_{cut} = 1.5w$ mm, which minimizes the reflection caused by impedance changes at corners. In the co-simulation, this structure is used to adjust the phase response of circulators and conductors. For circulators, its electrical length is set to ensure that the phase change of the electromagnetic wave after passing through two of the structures and one circulator is 0. And for conductors, it introduces an additional electrical length of π along the

direction parallel to the junction.

Figure 16d shows the unit of the rectangular lattice conductor with $w_1 = 2.2$ mm, $w_2 = 1.8$ mm, $l_1 = 49.9$ mm and $l_2 = 50.8$ mm.

S-parameters among the corresponding ports of the four components are separately simulated. Subsequently, the components are utilized to construct the junction model in CST design studio for microwave field-circuit co-simulation. The results are presented as the red squares in Fig. 3b in the main text.

VII. KWANT SIMULATION

In this section, we firstly introduce the details about simulating the transport of the topological junction with Kwant [18]. Then, in order to realize nearly equivalent scattering properties of a semi-infinite conductor with finite size, the details about imaginary absorbing potential are provided.

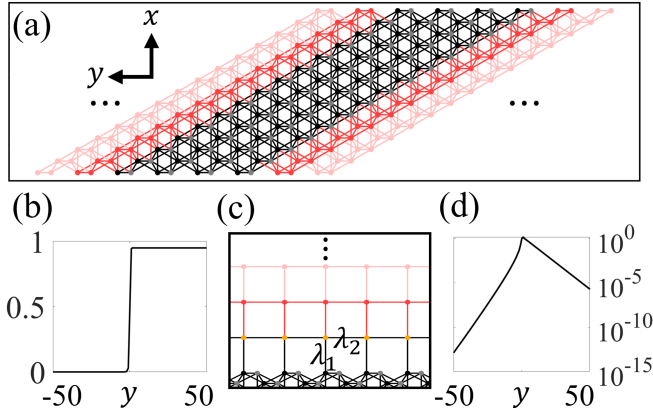


FIG. 17. (a) The Kwant simulation model of Haldane ribbon with armchair boundaries. Black and grey sites represent for sublattice A and B, respectively. Red lattice stands for the infinite extension along both directions of y . (b) Response profile of 101 sites on the upper boundary of (a) when excited at the center. (c) The semi-infinite conductor attached to sublattice A of the Haldane ribbon. λ_1 and λ_2 are the hopping of the conductor lattice along x and y , respectively. (d) Response profile of the same region and excitation as (b) after the attachment of the conductor.

A. Topological junction

To demonstrate the non-bloch transport of topological insulator-conductor junction, Kwant, a open source Python package, is adopted. Firstly, the simulation model of a Haldane ribbon with armchair boundaries is constructed (Fig. 17a). The corresponding hoppings are set to be $t_1 = t_2 = 1$. Transport properties of the topological insulator are simulated by calculating the Green's function of the upper side for 101 lattice sites. When excited at the center, the response of all sites is depicted as Fig. 17b, which represents for the chiral boundary state of Haldane model. Based on the Haldane ribbon, a semi-infinite conductor with square lattice is attached to sublattice A to construct the junction (Fig. 17c). Hopping parameters of the conductor lattice are set to be $\lambda_1 = 1$ and $\lambda_2 = -0.9$. Transport properties of the junction are simulated in the same way and at the same region as above. The corresponding response is shown as Fig. 17d. In Fig. 17b, waves cannot propagate along $-y$ because of the boundary state being anticlockwise. However, in Fig. 17d, waves decay exponentially at different rates in different directions, which represents for the non-bloch transport and can be attributed to the non-Hermiticity introduced by the Hermitian semi-infinite conductor.

B. Imaginary absorbing potential

Constructing the junction needs for a semi-infinite conductor that is impractical for experimental setup. Therefore, imaginary potential method [19, 20] is adopted on

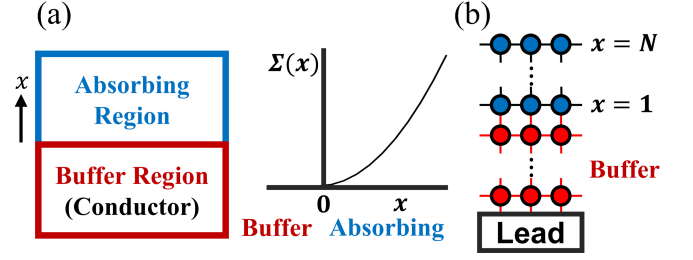


FIG. 18. (a) Schematic of the imaginary potential method. (b) Kwant model used to optimize the controlling parameters. A lead is attached to the bottom to simulate the reflection.

a finite conductor to realize equivalent effects as a semi-infinite one. As shown in Fig. 18a, the method consists of two regions. In absorbing region, imaginary onsite potential is introduced to the lattice sites to absorb the waves propagating towards the end. Moreover, a buffer region is used to extend the propagation time of the ineluctable backscattering wave so that it would not influence the transportation of the topological junction in certain simulation time. According to Ref. [19], a polynomial form of imaginary onsite potential is adopted:

$$\Sigma(x) = i(n+1)Ax^n, \quad (59)$$

where n and A are controlling parameters, and x is the order number counted from the start point of the absorbing region (Fig. 18b). Generally, the values of imaginary potential should be large enough so that the waves can be absorbed within a region as small as possible. However, sharp change of the values from one point to the next causes backscattering that weakens the absorption. Thus, the actual problem is the optimization about controlling parameters n , A , and the length of the buffer and absorbing region in x . To obtain appropriate parameters, a finite square lattice with imaginary onsite potential according to Eq. 59 is constructed in Kwant (Fig. 18b). The number of sites in each layer is 15 according to the experimental design and the length of the buffer region in x is 5 layers. A lead is attached to the lattice to simulate the reflection. At a fixed length N of the absorbing region, parameter sweep of n and A is performed to minimize the reflection. The same process is executed for different values of N . Finally, for circuit experiment parameters of $\lambda_1 = -1$, $\lambda_2 = 0.1$, we choose the controlling parameters as $N = 5$, $n = 1.8$ and $A = 0.025$, with a reflectivity less than 1%.

VIII. EXPERIMENTAL DETAILS

In this section, we give details about the experimental setup of the circuits topological junction. The junction can be divided into two parts, namely, topological insulator circuits and conductor circuits as shown in Fig. 19a. Both of them are manufactured through printed circuit boards (PCBs), and then connected together.

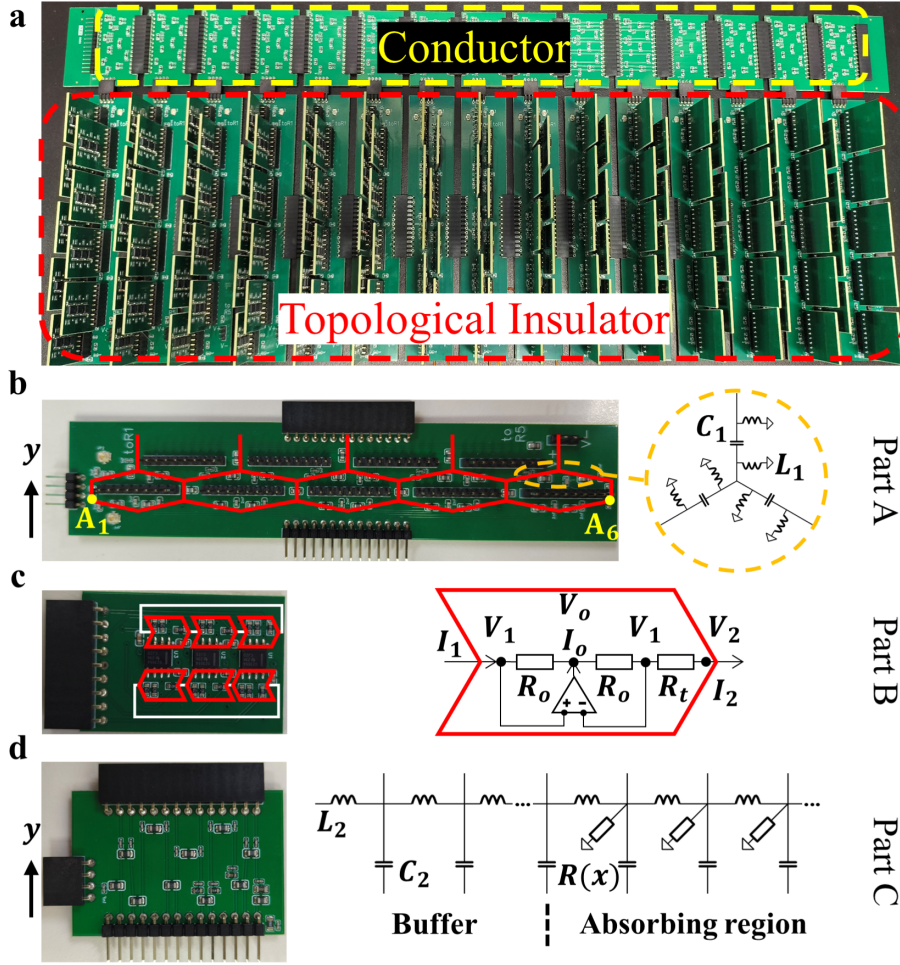


FIG. 19. Experimental setup of the circuit topological junction. (a) The junction consists of topological insulator and conductor. (b) Part A is used to construct the honeycomb lattice. The inset shows the configuration of LCL resonance couple. In experiment, the voltage on site A_1 is measured. (c) Part B realizes the non-reciprocal coupling t_2 within a single hexagon, which consists of six INICs. (d) Part C constructs the conductor with buffer and absorbing region.

A. Circuit realization of Haldane model

The circuit Haldane model consists of two kinds of PCBs, corresponding to the honeycomb lattice and the next-nearest-neighbor (NNN) hoppings within a single hexagon unit, respectively. Figure 19b shows the PCB of honeycomb lattice, which is referred to as part A for convenience. The nearest-neighbor hopping amplitude of $t_1 = 1$ is achieved through an inductor-capacitor-inductor (LCL) resonance couple, with $L_1 = 3.5 \mu\text{H}$ and $C_1 = 1 \text{ nF}$. Figure 19c shows the PCB of NNN hoppings (referred to as part B). We use three two-gate operational amplifiers (OPA2365, Texas Instruments) in each to construct six negative impedance converters with current inversion (INICs). The structure of INIC is shown on the right of Fig. 19c. An INIC leads to $-I_1 = I_2$ [21], which means a negative resistance $-R_t$ from node 1 to node 2 and a positive resistance R_t from node 2 to node 1, thus introducing the non-reciprocal coupling.

The NNN hopping amplitude of $t_2 = 1/6$ is achieved through a resistor of $R_t = 348 \Omega$ as the effective resistor of an INIC. When constructing the Haldane model, 15 pieces of part A are connected along y -direction, then 131 pieces of part B are inserted on them. Additionally, the site A_6 of each part A is grounded with a resistor of 27Ω in order to eliminate the reaching voltage signals through the edge state, thus simulating the infinite length along y -direction.

The tolerance of resistors, capacitors and inductors are 0.1%, 1%, and 5%, respectively.

B. Circuit realization of the semi-infinite conductor

Figure 19d shows the PCB of the conductor (referred to as part C). It consists of buffer (5 layers) and absorbing region (5 layers). The corresponding parameters of circuit components are $L_2 = 3.5 \mu\text{H}$ (for $\lambda_1 = -1$), $C_2 = 100 \text{ pF}$ (for $\lambda_2 = 0.1$), $R(6) = 820 \Omega$, $R(7) = 237 \Omega$,

$R(8) = 115 \Omega$, $R(9) = 68 \Omega$, and $R(10) = 45.3 \Omega$. Additionally, each node of absorbing region is also grounded with a capacitor of 470 pF to adjust the onsite potential. When constructing the topological junction, 15 pieces of part C are connected along y -direction, and then inserted to the top edge of the Haldane circuit.

The tolerance of resistors, capacitors and inductors are 0.1%, 1%, and 5%, respectively.

C. Measuring of the non-Bloch transport

Before measuring, a DC power supply (E36311A, Keysight) is connected to corresponding electrodes on the PCBs to supply the operational amplifiers and activate the INICs. Subsequently, a waveform generator (33220A, Agilent) delivering a 2.7 MHz sinusoidal signal is connected to site A_1 of the 14th part A as the excita-

tion source. This signal is simultaneously routed a lock-in amplifier (HF2LI, Zurich Instruments) as a reference for high-resolution detection.

The propagation characteristics along the negative y -direction of the junction are measured by sequentially measuring voltage signals at A_1 from the 13th to the 4th part A using the lock-in amplifier. Conversely, the positive y -direction propagation are determined by exciting A_1 of the 2nd part A and measuring responses from the 3rd to the 12th. The amplitude of all the acquired signals are normalized to the source.

Notably, the frequency-locking capability of the lock-in amplifier enables selective retention of target signals, namely, signals with the same frequency as the excitation, while effectively suppressing extraneous noise of the setup and offset voltage of the operational amplifiers. This methodology facilitates reliable detection of weak signals at the sub-microvolt level.

-
- [1] S. Datta, *Electronic transport in mesoscopic systems* (Cambridge university press, 1997).
 - [2] A. Alase, E. Cobanera, G. Ortiz, and L. Viola, Exact solution of quadratic fermionic hamiltonians for arbitrary boundary conditions, *Phys. Rev. Lett.* **117**, 076804 (2016).
 - [3] E. Cobanera, A. Alase, G. Ortiz, and L. Viola, Exact solution of corner-modified banded block-toeplitz eigen-systems, *J. Phys. A: Math. Theor.* **50**, 195204 (2017).
 - [4] A. Alase, E. Cobanera, G. Ortiz, and L. Viola, Generalization of bloch's theorem for arbitrary boundary conditions: Theory, *Phys. Rev. B* **96**, 195133 (2017).
 - [5] V. Kaladzhyan and C. Bena, Obtaining majorana and other boundary modes from the metamorphosis of impurity-induced states: Exact solutions via the t-matrix, *Phys. Rev. B* **100**, 081106 (2019).
 - [6] S. Pinon, V. Kaladzhyan, and C. Bena, Surface green's functions and boundary modes using impurities: Weyl semimetals and topological insulators, *Phys. Rev. B* **101**, 115405 (2020).
 - [7] Y. Hatsugai, Chern number and edge states in the integer quantum hall effect, *Phys. Rev. Lett.* **71**, 3697 (1993).
 - [8] V. Dwivedi and V. Chua, Of bulk and boundaries: Generalized transfer matrices for tight-binding models, *Phys. Rev. B* **93**, 134304 (2016).
 - [9] R. S. K. Mong and V. Shivamoggi, Edge states and the bulk-boundary correspondence in dirac hamiltonians, *Phys. Rev. B* **83**, 125109 (2011).
 - [10] M. Wimmer, *Quantum transport in nanostructures: From computational concepts to spintronics in graphene and magnetic tunnel junctions*, Phd thesis, University of Regensburg, Regensburg (2009).
 - [11] D. H. Lee and J. D. Joannopoulos, Simple scheme for surface-band calculations. ii. the green's function, *Phys. Rev. B* **23**, 4997 (1981).
 - [12] M. Wu, Q. Zhao, L. Kang, M. Weng, Z. Chi, R. Peng, J. Liu, D. H. Werner, Y. Meng, and J. Zhou, Evidencing non-bloch dynamics in temporal topoelectrical circuits, *Phys. Rev. B* **107**, 064307 (2023).
 - [13] M. Wu, M. Weng, Z. Chi, Y. Qi, H. Li, Q. Zhao, Y. Meng, and J. Zhou, Observing relative homotopic degeneracy conversions with circuit metamaterials, *Phys. Rev. Lett.* **132**, 016605 (2024).
 - [14] D. Youla, L. Castriota, and H. Carlin, Bounded real scattering matrices and the foundations of linear passive network theory, *IRE Transactions on Circuit Theory* **6**, 102 (1959).
 - [15] J. Helszajn, Waveguide and stripline 4-port single-junction circulators (short papers), *IEEE Transactions on Microwave Theory and Techniques* **21**, 630 (1973).
 - [16] J. Helszajn, M. McKay, and I. Macfarlane, Complex gyrator circuit of 4-port single junction circulator, *IEEE microwave and wireless components letters* **14**, 40 (2004).
 - [17] J. Helszajn, The adjustment of the m-port single-junction circulator, *IEEE Transactions on Microwave Theory and Techniques* **18**, 705 (1970).
 - [18] C. W. Groth, M. Wimmer, A. R. Akhmerov, and X. Waintal, Kwant: a software package for quantum transport, *New Journal of Physics* **16**, 063065 (2014).
 - [19] J. Weston and X. Waintal, Linear-scaling source-sink algorithm for simulating time-resolved quantum transport and superconductivity, *Phys. Rev. B* **93**, 134506 (2016).
 - [20] T. Kloss, J. Weston, B. Gaury, B. Rossignol, C. Groth, and X. Waintal, Tkwant: a software package for time-dependent quantum transport, *New Journal of Physics* **23**, 023025 (2021).
 - [21] T. Hofmann, T. Helbig, C. H. Lee, M. Greiter, and R. Thomale, Chiral voltage propagation and calibration in a topoelectrical chern circuit, *Phys. Rev. Lett.* **122**, 247702 (2019).